(2)

FERROELECTRIC TUNGSTEN BRONZE BULK CRYSTALS AND EPITAXIAL THIN FILMS FOR ELECTRO-OPTIC DEVICE APPLICATIONS

Semi-Annual Technical Report No. 4
For Period 4/01/84 through 9/30/84

FEBRUARY
~~JANUARY~~ 1985

DARPA Order No.	4540
Program Code:	P2D10
Name of Contractor:	Rockwell International Corporation
Effective Date of Contract:	09/30/82
Contract Expiration Date:	09/29/85
Contract Number:	N00014-82-C-2466
Principal Investigators:	Dr. R.R. Neurgaonkar (805) 373-4109
	Dr. L.E. Cross Pennsylvania State University (814) 865-1181

Sponsored by

Defense Advanced Research Projects Agency (DoD)
DARPA Order No. 4540
Monitored by Naval Research Laboratory
Under Contract No. N00014-82-C-2466

UNCLASSIFIED
SECURITY CLASSIFICATION OF THIS PAGE

REPORT DOCUMENTATION PAGE

1a. REPORT SECURITY CLASSIFICATION: Unclassified	1b. RESTRICTIVE MARKINGS
2a. SECURITY CLASSIFICATION AUTHORITY	3. DISTRIBUTION/AVAILABILITY OF REPORT: Approved for public release; distribution unlimited.
2b. DECLASSIFICATION/DOWNGRADING SCHEDULE	
4. PERFORMING ORGANIZATION REPORT NUMBER(S): SC5340.8SA	5. MONITORING ORGANIZATION REPORT NUMBER(S)
6a. NAME OF PERFORMING ORGANIZATION: Rockwell Internetionel Science Center; 6b. OFFICE SYMBOL (If applicable)	7a. NAME OF MONITORING ORGANIZATION
6c. ADDRESS (City, State and ZIP Code): 1049 Camino Dos Rios, Thousand Oaks, CA 91360	7b. ADDRESS (City, State and ZIP Code)
8a. NAME OF FUNDING/SPONSORING ORGANIZATION: Naval Research Laboratory; 8b. OFFICE SYMBOL (If applicable)	9. PROCUREMENT INSTRUMENT IDENTIFICATION NUMBER: Contract No. N00014-82-C 2466
8c. ADDRESS (City, State and ZIP Code): 4555 Overlook Avenue S.W., Washington, DC 20375	10. SOURCE OF FUNDING NOS. — PROGRAM ELEMENT NO.; PROJECT NO.: 4540; TASK NO.; WORK UNIT NO.
11. TITLE: FERROELECTRIC TUNGSTEN BRONZE BULK CRYSTALS AND EPITAXIAL THIN FILMS FOR ELECTRO-OPTIC DEVICE APPLICATIONS	
12. PERSONAL AUTHOR(S): Oliver, John R.	
13a. TYPE OF REPORT: Semi-Annual Technical Rpt; 13b. TIME COVERED: FROM 04/01/84 TO 09/30/84	14. DATE OF REPORT (Yr., Mo., Day): FEBRUARY 1985; 15. PAGE COUNT: 59

16. SUPPLEMENTARY NOTATION
The views and conclusions contained in this document are those of the authors and should not be interpreted as necessarily representing the official policies, either expressed or implied, of the Defense Advanced Research Projects of the U.S. Government.

17. COSATI CODES			18. SUBJECT TERMS (Continue on reverse if necessary and identify by block number)
FIELD	GROUP	SUB GR.	

19. ABSTRACT (Continue on reverse if necessary and identify by block number)

Several doped (Ce^{3+}/Ce^{4+} and Fe^{2+}/Fe^{3+}) and undoped SBN:60 single crystals have been grown by the Czochralski technique, and crystals as large as 2-2.5 cm in diameter have been successfully developed. The crystal quality and striations seem to depend strongly on the type of dopant incorporated. For example, Ce-doped SBN:60 crystals exhibit no striations with excellent optical quality, while Fe-doped SBN:60 crystals are heavily striated. The Ce-doped crystals seem to have promising device applications and, hence further work on this crystal is in progress to optimize its photorefractive properties. Since the crystals have been grown in an oxygen atmosphere, it is difficult to predict whether both valance states such as Ce^{3+}/Ce^{4+} are present. Therefore, future work will include the determination of dopant valance states and their effect on photorefractive sensitivity and speed.

Work on the flux system $Pb_2V_2O_7$-$Ba_2V_2O_7$-$PbNb_2O_6$-$BaNb_2O_6$ has shown that only the rhombohedral PBN phase can be precipitated, even when quenching to room temperature from 1250°C. However, work on the pseudo-binary systems BaV_2O_6-PBN:60 and $Pb_{1-x}Ba_xV_2O_6$-PBN:60 has resulted in the formation of

Over

20. DISTRIBUTION/AVAILABILITY OF ABSTRACT: UNCLASSIFIED/UNLIMITED ☒ SAME AS RPT. ☐ DTIC USERS ☐	21. ABSTRACT SECURITY CLASSIFICATION: Unclassified
22a. NAME OF RESPONSIBLE INDIVIDUAL	22b. TELEPHONE NUMBER (Include Area Code); 22c. OFFICE SYMBOL

DD FORM 1473, 83 APR — EDITION OF 1 JAN 73 IS OBSOLETE.

UNCLASSIFIED
SECURITY CLASSIFICATION OF THIS PAGE

the farroelectric tetragonal PBN phase, and furthar research is being conducted on these systems to astablish melting temperatura and supercooling range.

Maasurements on the photorafractiva effect in undoped and Ce-doped SBN:60 crystals hava shown a 5.5 increase in tha two-beam coupling coefficiant for Ca-doped material, but with a similar rasponse time 0.12 s A bend conduction transport model is presented which indicates that response tima may be reduced to 0.01 s or less by a decrease of the number of empty acceptor traps, N_A, perhaps by means of crystal annealing in a partially reducing atmosphara.

Additional keywords: tungsten bronzes, impurities.

TABLE OF CONTENTS

LIST OF FIGURES

LIST OF FIGURES

LIST OF TABLES

1.0 SUMMARY AND PROGRESS

Tungsten bronze (T.B.) family crystals have been shown to be useful for a number of device applications, including electro-optics, nonlinear optical, pyroelectric and high frequency dielectrics. The current work reports on the development of good quality (acceptable for proposed device studies) $Sr_{1-x}Ba_xNb_2O_6$, where x = 0.40 and 0.50, and morphotropic phase boundary (MPB) compositions. Considerable progress has been made in several areas, including the growth of Ce- and Fe-doped SBN:60 crytals and the characterization of their ferroelectric and photorefractive properties. Based on current work, a number of new dopants have been identified for future investigation. This work also includes the continued effort to search for new T.B. systems and to identify MPB compositions for pyroelectric, electro-optic and photorefractive applications.

Several doped (Ce^{3+}/Ce^{4+} and Fe^{2+}/Fe^{3+}) and undoped SBN:60 single crystals have been grown by the Czochralski technique, and crystals as large as 2-2.5 cm in diameter have been successfully developed. The crystal quality and striations seem to depend strongly on the type of dopant incorporated. For example, Ce-doped SBN:60 crystals exhibit weak or no striations with excellent optical quality, while Fe-doped SBN:60 crystals are heavily striated and have generally poor optical quality. Efforts are under way to establish the parameters that control the growth of these doped crystals and thereby improve their quality. The photorefractive properties of Ce-doped crystals can be evaluated effectively. The crystals seem to have promising device applications. Since the crystals have been grown in an oxygen atmosphere, it is difficult to predict whether both valence states such as Ce^{3+}/Ce^{4+} and Fe^{2+}/Fe^{3+} are present. Therefore, future work will include the determination of dopant valence states and their effect on the photorefractive properties.

Annealing studies on undoped SBN:60 crystals have shown that significant changes occur in the dielectric properties with changes in the cooling rate. Faster cooling rates appear to freeze in a narrower distribution of localized site preferences of the Sr and Ba ions, resulting in a closer ap-

proximation to first order ferroelectric transition behavior and a significant reduction in tan . No significant change of the Curie temperature was observed, so that the recent slight increase observed (5-7°C) must be attributed instead to the use of higher purity starting materials.

Extensive work has been performed on the flux systems required for LPE thin film growth of SBN and $Pb_{1-x}Ba_xNb_2O_6$ (PBN) bronze compositions. Phase diagram work on the system SrV_2O_6-BaV_2O_6-$SrNb_2O_6$-$BaNb_2O_6$ has determined that SBN:75 films can be grown from flux compositions which cover a relatively limited range in the phase diagram, and with a relatively high melting point (> 1350°C). Work on the flux system $Pb_2V_2O_7$-$Ba_2V_2O_7$-$PbNb_2O_6$-$BaNb_2O_6$ has shown that only the rhombohedral PBN phase can be precipitated, even when quenching to room temperature from 1250°C. However, work on the pseudo-binary systems BaV_2O_6-PBN:60 and $Pb_{1-x}Ba_xV_2O_6$-PBN:60 has resulted in the formation of the ferroelectric tetragonal PBN phase, and further research is being conducted on these systems based on these encouraging results.

Research has continued on the pseudo-binary morphotropic bronze systems $Ba_2NaNb_5O_{15}$-$Sr_5NaNb_5O_{15}$ (BNN-SNN) and $Pb_2KNb_5O_{15}$-$Ba_2NaNb_5O_{15}$ (PKN-BNN). Improved sintering of ceramic compositions from these systems has resulted in significantly improved dielectric properties, particularly near morphotropy. Lattice constant evaluation of the BNN-SNN system has shown that two independent pseudo-tetragonal (mm2) phases exist adjacent to the morphotropic phase boundary, with an abrupt discontinuity in the Curie-Weiss coefficient occurring at this point. The system PKN-BNN shows particularly dramatic changes in dielectric properties near the morphotropic 0.75 PKN-0.25 BNN composition, with an abrupt discontinuity in the b and c lattice parameters, indicating the potential for particularly enhanced piezoelectric and electro-optic properties. The system changes from a second order ferroelectric transition (orthorhombic) to first order (tetragonal) with composition, with a steep decline in the Curie-Weiss coefficient. Single crystal Czochrolski growth of selected compositions from these systems will now be attempted.

An extensive discussion of the thermodynamic phenomenology for tungsten bronze crystals is presented along with a tabulation of a number of thermodynamic constants based on current research and other data in the literature. An excellent fit to birefringence polarization data for $Ba_2NaNb_5O_{15}$ (BNN) is found for the Devonshire form of the Gibbs free energy expansion, and good agreement is found for a number of thermodynamic constants over a broad range of tungsten bronze materials. This indicates that the hypothesis of near-constant higher order stiffness parameters is a good approximation for tetragonal bronze ferroelectrics, thereby allowing the analysis of a very wide range of other bronze compositions.

Measurements on the photorefractive effect in undoped and Ce-doped SBN:60 crystals at Cal Tech have shown a 5.5 increase in the two-beam coupling coefficient for Ce-doped material, but with a similar response time of 0.12 s. A band conduction transport model is presented which indicates that response time may be reduced to 1 ms or less by a decrease of the number of empty acceptor traps, N_A, perhaps by means of crystal annealing in a partially reducing atmosphere.

2.0 DEVELOPMENT OF OPTICAL QUALITY SBN CRYSTALS

2.1 Material Growth Techniques

Most of the bronze compositions grown in our laboratory are based on solid solution systems; therefore suitable growth techniques to produce crystals free of optical defects such as striations, scattering centers and twinning must be developed. Striations and other defects are typical problems common to solid solution crystals, and it is often difficult to suppress them completely. However, these problems can be reduced effectively such that the crystals can be useful for optical device studies. The difficulty of this task underscores the criticality of selecting appropriate growth techniques in the present work. At present, three different techniques have been chosen to develop SBN and other bronze crystals. They are as follows:

1. Bulk Single Crystals: Czochralski technique
2. Thin Films: Liquid phase epitaxy (LPE)
3. Strip Crystals: Edge defined film-fed technique

The first two techniques are well established in our current work, and bulk crystals and films of SBN compositions have already been grown. In the present report, the continued growth of striation-free SBN crystals and films is discussed along with associated growth problems.

2.2 Growth Procedure

Nb_2O_5, $SrCO_3$, Fe_2O_3, CeO_2 and $BaCO_3$ fine powders have been used as starting materials and have been weighed out in the desired proportions, as summarized in Table 1. The batch mixture is ball-milled in acetone for 20-30 h, and then is poured into a large drying dish. The dried powder is placed in a platinum reaction dish and is calcined at 1000°C for 10-15 h to eliminate carbonates and any possible carbon from the pyrolytic breakdown of residual acetone. The calcine powder is then ball-milled and refired in an oxygen flow of 2 cfh at 1400°C

Table 1

Materials for Bulk Single Crystal SBN:60 Growth

Crystal Composition	Starting Materials		Conditions and Remarks
SBN:60	a. $SrCO_3$	135.08 gms	Congruent melting composition
	b. $BaCO_3$	115.48 gms	Large crystals can be grown
	c. Nb_2O_5	398.73 gms	Large electro-optic coefficient (r_{33})
	Total wt.	649.26 gms	Melts at 1510°C
	Growth wt.	450.00 gms	Crack-free and optical quality
SBN:60 + Fe^{3+}	a. $SRCO_3$	135.08 gms	Dielectric and electro-optic
	b. $BaCO_3$	115.48 gms	coefficient increased
	c. Nb_2O_5	398.73 gms	Growth of large crystals is
	d. Fe_2O_3	1.98 gms	possible
		to	Enhanced photorefractive
		3.05 gms	properties
	Total wt.	651.24 gms	Crack-free crystals
	Growth wt.	450.00 gms	
SBN:60 + Ce^{3+}	a. $SrCO_3$	135.08 gms	Dielectric and electro-optic
	b. $BaCO_3$	115.48 gms	coefficient improved
	c. Nb_2O_5	398.73 gms	Growth of large crystals is
	d. CeO_2	1.00 gms	possible
		to	Enhanced photorefractive
		1.50 gms	properties
	Total wt.	650.26 gms	Crack-free and optical quality
	Growth wt.	450.00 gms	crystals

for about 4-6 h. Phase checks and x-ray lattice constant measurements are made for each batch to ensure the use of a phase-pure bronze composition for crystal growth. A thick-walled platinum crucible of 2 × 2 in. in dimension is used for this growth, and this container holds roughly 450 g of melt composition.

2.3 Growth of Undoped SBN:60 Crystals

As summarized in Table 2, we have grown a number of undoped SBN:60 single crystals of excellent quality using the Czochralski technique. The growth process appears to be highly reproducible for this composition. Since the automatic diameter control (ADC) system is now well established to control the striation problem more effectively, we have begun to introduce a few more changes in the current system to improve the crystal quality further.

Recently, we found that small amounts of impurities have a drastic photorefractive effect in optical waveguide applications. Current optical measurements at NRL on SBN:60 crystals indicate that the elimination of impurities should significantly improve the optical quality for waveguide applications. In view of this, higher grade starting materials have been used in our current growth experiments. Although minor changes in thermal gradients have occurred, this batch has been used to successfully grow several new SBN:60 crystals. The quality of these crysals is significantly better; thus by controlling the thermal gradients more effectively, further improved optical quality should be possible. During the next six months we expect to have a sufficient number of crystals to analyze the crystal quality and thereby to further refine the growth technique.

2.4 Growth of SBN:50 Crystals

This composition was originally selected in the present work to use as substrate material for the LPE growth of bronze compositions. Since SBN:50 exhibits large pyroelectric and electro-optic coefficients, and since the Curie temperature for this crystal is over 120°C, it is important that this crystal be further developed. However, growth is rather difficult as compared to the congruent melting composition, SBN:60, due to cracking while cooling through the paraelectric/ferroelectric phase transition temperature. In our earlier experiments, SBN:50 crystals were grown without using the ADC system.

Table 2

Growth of SBN:60 Crystals

Boule No. 2	Date Grown	Boule wt.	Dip °C	Rotation rpm	Remarks, Observations
185	05/29/84	16.7	1491	5-8	Uncracked
186	06/01/84	34.6	1489	~ 6	Neck nearly defect-free
187	06/06/84	38.3	1491	~ 8	ADC used, uncracked
188	06/12/84	25	1482	5-15	New charge - flat top, heavily defected, cracks 5 nines purity - less color
189*	06/18/84	25.3	1484	~10	Uncracked - appears core-free
190	06/21/84	18.6	1485	10-12	Uncracked - core-free
191	07/10/84	27.8	1485	8-10	Uncracked - had to de-twin
192	07/13/84	14.3	1486	10	One deep twin - cracked along one side
193	07/30/84	27	1480	~12	Minor coring, uncracked
194	08/02/84	38	1485	10	Good ADC, uncracked core-free boule
195*	08/23/84	42.5	1485	~10	1.8-1.9 cm dia, uncracked
196	08/27/84	49	1485	10	2.0 cm dia, uncracked
197	08/30/84	29	1490	10	Uncracked
198	09/11/84	~5	1490	10	Test new load cell (test crystal)
199	09/25/84	29.5	1485	12	Test new crucible support (small boule)
200	09/28/84	52.5	1485	5-10	Small bubble in boule neck ~19 mm dia
201	10/03/84	41	~1485	5-10	Pink color boule, 19 mm dia
202	10/05/84	41	~1485	5-10	Pink color, 18 mm dia Minor twinning
203	10/10/84	18	~1485	~10	Pink, uncracked
204	10/18/84	35.7	~1485	5-10	Dark pink, no twins, uncracked
205	10/30/84	~15	~1485	10-15	Wine color, uncracked

*To NRL

Results for SBN:60 crystal growths indicate that the use of this system is instrumental in suppressing temperature fluctuations in the melt. Using such an up-graded technique should minimize crystal cracking greatly. Furthermore, we are also using ultra-pure starting materials for this growth so that we can eliminate cracking due to foreign cations. We have already demonstrated the growth of SBN:50 up to 1 cm in diameter without using the ADC system, and this indicates that we should be able to further improve the size and quality of this crystal for pyroelectric thermal detector applications. Once this technique is well established for undoped crystals, we may introduce La^{3+} in order to enhance the pyroelectric response, as the benefits from the substitution of La^{3+} in SBN are well known (Liu, et al[13]).

2.5 Effects of Annealing on the Dielectric Properties of SBN:60

In the unfilled T.B. structure, both the Sr^{2+} and Ba^{2+} cations are distributed over the 15- and 12-fold coordinated sites. The influence of this site distribution on the dielectric properties, particularly below the Curie temperature, T_c, is not known to any great degree, however. The possibility arises that one might be able to influence the dielectric properties of SBN through changes in the high temperature annealing procedures used for this ferroelectric bronze. This interest was spurred further by the observation of an increase in T_c and the room temperature dielectric constant for recent SBN:60 crystal growths. These high-purity growths have shown a Curie temperature of 77-79°C, compared to earlier 71-73°C values, and a room temperature dielectric constant of 900-950, in contrast with poled values of 500-700 for earlier growths. Both post-growth annealing procedures and melt impurity content could play a role in these differences.

We decided to examine the effects of the annealing procedure on a recent, high-purity SBN:60 crystal. Specifically, the crystal was annealed at 1400°C in pure oxygen for four hours - typical of our current procedure - and then was cooled at two different rates of 50°C/h and 200°C/h. The c-axis sample was then poled at 7.5 kV/cm and the dielectric properties were

measured. The results for these experiments are tabulated in Table 3. The Curie temperature T_c did not change appreciably, but other properties such as the Curie-Weiss coefficient C_c, the dielectric constant, and the dielectric loss are seen to be influenced considerably by the cooling rate.

Table 3
Annealing Effects on Poled SBN:60 (c-cut)

Cooling Rate	T_c (°C)	C_c (°C)	ε_r at T_c	ε_r at 23°C	tanδ at 23°C
50°C/h	77	3.87×10^5	59,700	978	0.0041
200°C/h	79	4.27×10^5	69,100	906	0.0020

Compared to the results for a 50°C/h rate, the data for a 200°C/h rate show significantly higher values for C_c and ε_r at the Curie temperature, but lower values for tanδ and ε_r at room temperature. The last point is particularly curious, since intuitively one would expect a higher value of ε_r at room temperature from the higher Curie-Weiss coefficient. But in fact, the 200°C/h rate produced a room temperature dielectric constant 8% lower than that for the 50°C/h rate. These data are highly reproducible, in that a given annealing procedure did not influence the results of any subsequent annealing test.

Several tentative conclusions can be drawn from these data. First, the higher cooling rate tends to "freeze-in" the ionic site preference distribution at a higher effective temperature than does the slower cooling rate. Because of this, one expects that the site preference distribution will be statistically narrower in the high cooling rate case, with a resultant decrease in the distribution of localized T_c values about the nominal value of 79°C. As a result, the dielectric characteristics below the Curie temperature

will be slightly closer to near-ideal first order phase transition behavior, with a corresponding decrease of ε_r at room temperature -- this in spite of the observed 10% increase in the Curie-Weiss coefficient. However, the effect observed here is relatively small. Perhaps of far greater significance is the factor of two decrease of tanδ in the high cooling rate case; this may also be tentatively associated with a reduction of the site preference distribution. If so, further reductions of the already moderately low tanδ values in SBN:60 may be possible.

The recently observed increase of T_c for SBN:60 crystals is not associated primarily with post-growth annealing procedures. A more likely explanation is the fact that recent SBN Czochralski growths have utilized high-purity starting materials (99.999%); it is well known that impurities such as iron, for example, can significantly lower the Curie temperature of SBN. The nearly 50% increase of the room temperature dielectric constant for the higher purity crystals remains puzzling; although permittivity values for the higher purity crystals are highly uniform from growth to growth, in contrast with the wide scatter observed for earlier growths. Hence, these results for SBN:60 cannot be considered conclusive, but must await further growths and experiments, particularly with regard to the effect of low-level dopants on the room temperature dielectric properties and Curie-Weiss behavior.

2.6 Growth of Doped SBN:60 Crystals

The main objective of this task is to enhance the photorefractive sensitivity and speed of ferroelectric SBN:60 single crystals using specific impurity species. The current trend in ferroelectric materials indicates that the photorefractive sensitivity of SBN:60 is very large, on the order of 10^{-3} or higher. However, the response time for these crystals is relatively slow when compared with the best known nonferroelectric cubic $Bi_{12}SiO_{20}$ (BSO) crystals, which have a response time typically on the order of 1 ms.

In order to improve response time and sensitivity, considerable progress has been made using appropriate dopants in materials such as SBN:60,

$KNbO_3$, $BaTiO_3$, and $LiNbO_3$. The most commonly used dopants in these crystals include Fe^{2+}/Fe^{3+}, Ce^{3+}/Ce^{4+}, Mo^{4+}/Mo^{6+}, and U^{4+}/U^{6+}. To develop high sensitivity and fast response in tungsten bronze SBN:60 crystals, effort has focussed on the increase of the space charge field, E, since the change in refractive index, Δn, is linearly proportional to E from the relation

$$\Delta n = 1/2\, n_i^3 r_{ij} E_j \quad ,$$

where r = electro-optic coefficient.

Table 4 summarizes the various dopants selected in the present study, their valence states, and their anticipated site preferences in the tungsten bronze structure. Since the role of Fe^{2+}/Fe^{3+} and Ce^{3+}/Ce^{4+} has been widely studied in various ferroelectric crystals, the present work has concentrated on these dopants. The growth and feasibility of SBN:60 crystals doped with these ions have been discussed in our previous report. Since then, considerable progress has been made to improve the quality of these crystals for potential use in photorefractive device applications.

Table 4
Role of Dopants in SBN:60 Crystals

	Site Preference						T_c	Dielectric	
Dopant	15-fold	12-fold	9-fold	6-fold	Configuration	Basic	°C	Constant	
Ce^{3+}	-	Ce^{3+}	-	-	$4f^1 5s^2 p^6$	$^2F_{5/2}$	Reduced	Increased	Large Crystals
Ce^{4+}	-	Ce^{4+}	Ce^{4+}	Ce^{4+}	-	-	Reduced	Increased	Large Crystals
Fe^{3+}	-	-	-	Fe^{4+}	$3d^5$	$^6S_{5/2}$	Reduced	Increased	Large Crystals
Fe^{2+}	-	-	Fe^{2+}	Fe^{2+}	$3d^6$	$^5D_4$	-	Increased	Large Crystals
Cr^{3+}	-	-	-	Cr^{3+}	$3d^3$	$^4F_{3/2}$	-	-	-
Mn^{2+}	-	-	Mn^{2+}	Mn^{2+}	$3d^5$	$^6S_{5/2}$	-	-	-
Mn^{3+}	-	-	-	Mn^{3+}	$3d^4$	$^5D_0$			
Nb^{4+*}							Reduced	Increased	Large Crystals

*Nb^{5+} reduces to Nb^{4+} at high temperature.

Table 5 summarizes the growth conditions, dopant concentration, and crystal properties for these growths. Both Ce^{3+}- and Fe^{3+}-doped SBN:60 single crystals have been grown by the Czochralski technique equipped with automatic diameter control (ADC) system. Growth of these crystals has been successful, and crystals as large as 2 to 2.5 cm in diameter have now been grown. This is the first time such large size Ce^{3+}-doped or Fe^{3+}-doped SBN:60 single crystals of excellent quality have been grown for photorefractive studies. The addition of these dopants in the SBN:60 melts has a significant effect on thermal conductivity; however, necessary changes in the after-heater profile were made to correct this problem.

Table 5
Growth Data on Doped and Undoped SBN:60 Crystals

Property	SBN:60	Fe^{3+}-SBN:60 (0.01-0.10%)	Ce^{3+}-SBN:60 (0.01-0.05%)
Growth Temp (°C)	1510	1500	1520
Crystal Size (Diameter)	2 to 3 cm	2 to 2.3 cm	~ 2 cm
Color of Crystal*	Pale Yellow	1. Yellow to green (as-grown) 2. Deep yellow (after oxidizing)	1. Pale yellow to orange (as-grown) 2. Orange (after oxidizing)
Defects	Almost striation-free	Heavily striated	Weakly striated
Quality	Excellent	Moderate	Excellent
T_c (°C)	72	51, x = 0.1%	70, x = 0.01%
Dielectric Constant**	ε_{33} = 900	ε_{33} = 3400, x = 0.1%	ε_{33} = 1300, x = 0.01%

*The coloration depends strongly on the concentration of dopant.
**Enhancement in dielectric constant indicates proportional increase in electro-optic coefficient.

Figures 1 and 2 show Fe- and Ce-doped SBN:60 crystals grown along the c-axis. The Fe-doped SBN:60 crystals are pale yellow to deep green in color after growth, depending on the concentration of Fe in the crystals. However, all crystals changed to a deep yellow color after oxiding in oxygen at 1000°C. This result indicates that the addition of Fe^{3+} might be reducing Nb^{5+} to Nb^{4+}, or alternatively there may be a small amount of Fe^{2+} present; further work is necessary to confirm this. In the case of Ce-doped SBN:60 crystals, the crystal color is pink and it persists even after oxiding at 1000°C. In both cases, fracture-free and reasonable quality crystals have been grown by this technique. The crystal habit for these crystals is similar to undoped crystals, and it is based on 24-facets of four prisms: (100), (110), (120), and (130).

SC85-29887

Fig. 1 Fe-doped SBN:60 grown along the c-axis.

SC85-29888

Fig. 2 Ce-doped SBN:60 grown along the c-axis.

In the present work, the Curie temperature, T_c, and dielectric properties of these crystals have been obtained by measuring capacitance and conductivity as a function of temperature. The technique is relatively simple and the measurements are made routinely using a computer-controlled capacitance bridge (HP 4274A). The test specimens used for the dielectric measurements are approximately 5-7 mm in diameter and 1-2 mm thick, and are coated on each side with platinum by a standard sputtering technique. Both the dielectric constant and T_c for Ce- and Fe-doped SBN:60 crystals are presented in Table 5. The results of these measurements show that T_c decreases for both dopants while the dielectric constant increases significantly, indicating a simultaneous increase of electro-optic coefficient αlong with an increase of the space charge field.

Optical evaluation of Ce- and Fe-doped SBN:60 crystals under a high resolution crossed-polarized microscope indicates that the Ce-doped SBN:60

crystals show minimum or no striations, while the Fe-doped SBN:60 crystals grown under similar conditions show a highly striated pattern. Figure 3 shows the striation patterns for both Ce- and Fe-doped SBN:60 crystals. The growth investigation indicates that the striation pattern can be controlled effectively by adjusting the pulling and rotation rates for the Ce-doped SBN:60 crystals, and the quality was found to be satisfactory for subsequent photorefractive studies, discussed in detail in Section 6.0. The existence of striations in the case of the Fe-doped crystals is clearly associated with the presence of Fe, since changes in the rotation or pulling rates had virtually no effect on the striation pattern. In the tungsten bronze structure, Ce^{3+} and Ce^{4+} are expected to occupy 12-fold coordinated sites, while Fe^{2+} and Fe^{3+} ions are expected to occupy the 6-fold coordinated site. Based on the present results, it seems that the striations depend strongly on the type of impurity cation and its location in the structure. This is an interesting piece of information, and we plan to pursue this in more detail. For the next six months the following aspects of SBN crystal growth will be studied:

- Establish the valence states of Ce in SBN:60 single crystals.
- Establish whether any free Nb^{4+} is present in SBN:60 crystals and its effect on photorefractive properties.
- Improve the current growth technique to suppress the striations present in Fe-doped SBN:60 crystals. Also establish the concentration at which the striations appear.
- Identify another suitable dopant which will occupy the 12- or 15-fold coordinate sites, e.g., Tb^{3+}/Tb^{4+}, Eu^{2+}/Eu^{3+}, or other cations.
- Establish the ferroelectric and electro-optic properties with respect to new dopants and evaluate their potential suitability in photorefractive applications.

SC85-29886

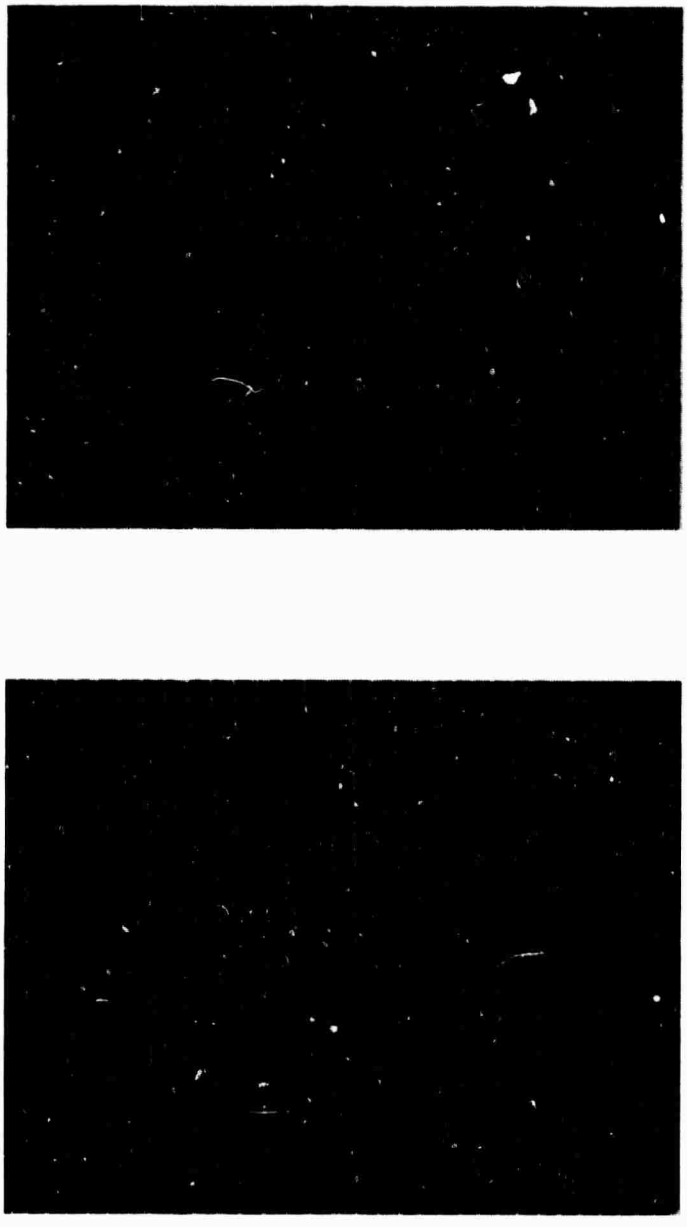

Fig. 3 Striation patterns for Ce-doped (upper) and Fe-doped (lower) SBN:60 crystals.

3.0 LIQUID PHASE EPITAXIAL GROWTH OF BRONZE COMPOSITIONS

3.1 Introduction

In our previous report, we described how to choose a proper flux composition for LPE growth of SBN:75 films on SBN:60 substrates by means of establishing the partial quaternary phase diagram SrV_2O_6-BaV_2O_6-$SrNb_2O_6$-$BaNb_2O_6$. Unfortunately, as a result, we found that the growth of SBN:75 films on SBN:60 may not be easy, since not only a relatively narrow range of suitable flux compositions must be dealt with, but also a necessarily high flux melting point (greater than 1350°C). Hence, our recent work has focussed on the LPE growth of SBN:50 on SBN:60 substrates.

For the LPE growth of bronze PBN:60 films on SBN:60 substrates, both the $Pb_2V_2O_7$-$Ba_2V_2O_7$-$PbNb_2O_6$-$BaNb_2O_6$ and PbV_2O_6-BaV_2O_6-$PbNb_2O_6$-$BaNb_2O_6$ flux systems have been studied. Only the nonferroelectric rhombohedral phase precipitated out for a Pb/Pb+Ba ratio greater than 60%. We have now extended our study in the flux system PbV_2O_6-BaV_2O_6-$PbNb_2O_6$-$BaNb_2O_6$ for Pb/Pb+Ba ratios less than 60%.

3.2 LPE Growth of SBN on c-cut SBN:60 Substrates

In previous work, we demonstrated that SBN:40 LPE films could be successfully grown on SBN:60 a-cut substrates. The same set-up has now been used for the growth of an LPE film on SBN:60 c-cut substrate, a 35% $Sr_{0.50}Ba_{0.50}Nb_2O_6$ + 65% BaV_2O_6 flux used for this study.

The flux was first melted at 1050°C. The c-cut SBN:60 substrate was dipped into the flux for 15 min and a 30 μm thick film was grown on the substrate, as shown in an edge view in Fig. 4. From the x-ray diffraction studies of the (002), (003) and (004) peaks (Fig. 5), clearly the composition of the film is different from that of the substrate (SBN:60), and is close to SBN:50 based on earlier single crystal results.

SC85-29889

Fig. 4 Edge view of a nominally SBN:50 epilayer grown on a c-cut SBN:60 substrate. Film thickness is 30 μm.

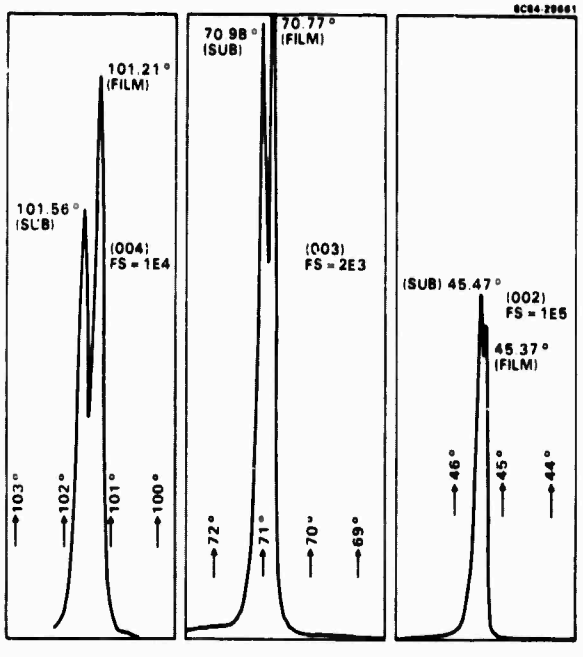

Fig. 5 X-ray diffraction peaks for SBN:50 epilayer and underlying SBN:60 substrate.

3.3 Flux Systems for PBN:60

Since we were previously unable to find either tetragonal or orthorhombic ferroelectric bronze phases in the $PbV_2O_6BaV_2$-O_6-$PbNb_2O_6$-$BaNb_2O_6$ system for a Pb/Pb+Ba ratio greater than 60%, we turned our attention to the other part of the phase diagram where the Pb/Pb+Ba ratio is between 20% and 60%. Table 6 lists several different flux compositions that have been studied in this region. Figure 6 shows the phase diagram results in which the solid circles represent the tetragonal bronze phase, the triangles represent the rhombohedral phase, and the squares represent other observed phases. This work shows that only in the shaded area of Fig. 6, which includes the flux compositions No. 3, No. 6, $Pb_{0.6}Ba_{0.40}Nb_2O_6$ and $Pb_{0.20}Ba_{0.80}Nb_2O_6$, can a single phase tetragonal bronze be formed.

Table 6
LPE Flux Systems for PBN

No.	Composition	Pb/Pb + Ba	Melting Temp (°C)	Remaining Phase
1	80% BaV_2O_6+ 20% $Pb_{0.5}Ba_{0.4}Nb_2O_6$	0.12	Melted, 1000°C	Other
2	70% BaV_2O_6 + 30% $Pb_{0.6}Ba_{0.4}Nb_2O_6$	0.18	Melted, 1000°C	Tet. PBN + $BaNb_2O_6$
3	50% BaV_2O_6 + 50% $Pb_{0.6}Ba_{0.4}Nb_2O_6$	0.30	Melted, 1250°C	Tet. PBN
4	65% BaV_2O_6 + 35% $Pb_{0.6}Ba_{0.4}Nb_2O_6$	0.21	Melted, 1000°C	Tet. PBN + Rhom PBN
5	65% $Pb_{0.4}Ba_{0.6}V_2O_6$ + 35% $Pb_{0.4}Ba_{0.6}Nb_2O_6$	0.40	Melted, 1000°C	Rhom PBN
6	50% $Pb_{0.4}Ba_{0.6}V_2O_6$ + 50% $Pb_{0.4}Ba_{0.6}Nb_2O_6$	0.40	Melted, 1100°C	Tet. PBN
7	50% $Pb_{0.5}Ba_{0.5}V_2O_6$ + 50% $Pb_{0.5}Ba_{0.5}Nb_2O_6$	0.50	Melted, 1150°C	Rhom PBN

SC84-26696

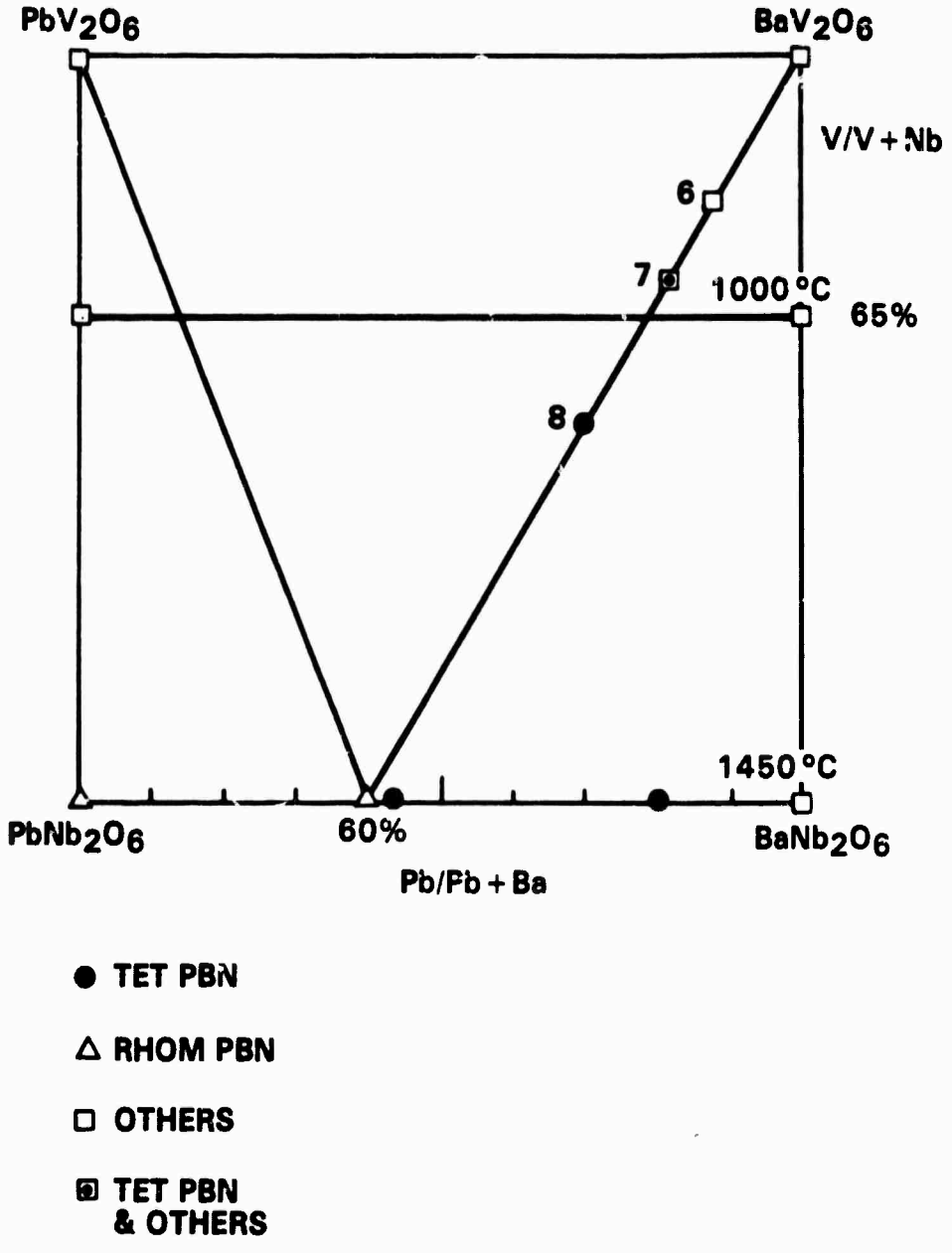

Fig. 6 PbV_2O_6-BaV_2O_6-$PbNb_2O_6$-$BaNb_2O_6$ phase diagram for LPE.

The LPE growth of PBN:60 films on SBN:60 substrates is currently in progress in our laboratory. The initial results indicate that the volatility of PbO will be a significant problem in the LPE growth process.

Future work will focus on the following:

- Lattice parameter standards for $Pb_{1-x}Ba_xNb_2O_6$.
- Establishment of suitable flux compositions for the LPE growth of PBN films.
- Determination of problems involved in the LPE growth process and required growth procedure modifications.

4.0 NEW TUNGSTEN BRONZE SYSTEMS FOR ELECTRO-OPTICS

Several of the more interesting tungsten bronze systems show morphotropic phase boundaries (MPB) which depend primarily on composition rather than on temperature. Ceramic or single crystal compositions adjacent to such boundaries show considerable enhancement of electro-optic, dielectric, piezoelectric, electromechanical and pyroelectric properties because of the proximity in energy of an alternate ferroelectric structure. In the present work, two such systems, $Ba_2NaNb_5O_{15}$-$Sr_2NaNb_5O_{15}$ and $Pb_2KNb_5O_{15}$-$Ba_2NaNb_5O_{15}$, have been investigated and are found to have MPB conditions with exceptionally high dielectric and other properties. In this report, we present further data on these bronze systems based on continued work.

4.1 $Ba_2NaNb_5O_{15}$-$Sr_2NaNb_5O_{15}$ System

Tungsten bronze barium sodium niobate (BNN) has been shown to be an outstanding material for electro-optic and nonlinear optic applications, particularly for second harmonic generation of near-IR laser radiation. The material was first discovered in 1967 by researchers at Bell Labs,[4-6] and was found to have a number of useful nonlinear optic and piezoelectric properties. Stoichiometric $Ba_2NaNb_5O_{15}$ is orthorhombic at room temperature with lattice constants a = 17.592Å, b = 17.626Å and c = 3.995Å, as determined from high angle x-ray measurements.[7] Above 260°C, an orthorhombic to tetragonal transformation occurs in which microtwinning is usually observed in single crystals, but with no significant dielectric anomalies. The Curie point is at approximately 570°C.

During this contact we began an investigation of the pseudo-binary system $Ba_2NaNb_5O_{15}$-$Sr_5NaNb_5O_{15}$ (BNN-SNN) in the search for new morphotropic phase boundary compositions at which enhanced piezoelectric, pyroelectric and electro-optic properties are anticipated. For ceramic material with a compositional variation (1-x)BNN-(x)SNN, a minimum in the Curie temperature was found for x = 0.60, at which T_c = 170°C, as discussed in the last report. Further measurements and data evaluation have now been done on this system, and a number of interesting features have been uncovered.

Figure 7 shows the computed least-squares lattice parameter evaluation for BNN-SNN based on an extensive series of powder x-ray measurements at room temperature. As seen in this figure, the c lattice constant varies almost linearly with composition over the entire range. In contrast, the a, and b parameters remain nearly constant up to a 0.60 SNN composition, at which point a discontinuity occurs. Because of the pseudo-tetragonal nature of the BNN-SNN system, it is very difficult to establish from powder x-ray data whether or not a true tetragonal or orthorhombic structure exists near this point. However, two independent pseudo-tetragonal phases exist near x = 0.60, which is also reflected in the Curie-Weiss dielectric behavior for this system. Examination of the Curie-Weiss coefficient, C_c, shows an abrupt discontinuity at x = 0.60, as shown in Fig. 8. The dielectric behavior for sintered ceramic samples remains first order ($\theta < T_c$) over the entire compositional range, with θ values varying smoothly with composition, as shown in Fig. 9.

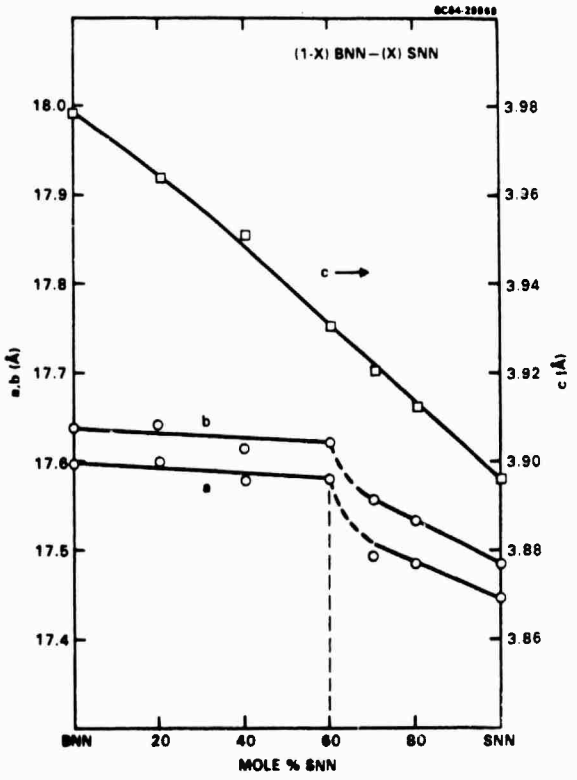

Fig. 7 Lattice parameters vs composition for the system (1-x)BNN-(x)SNN.

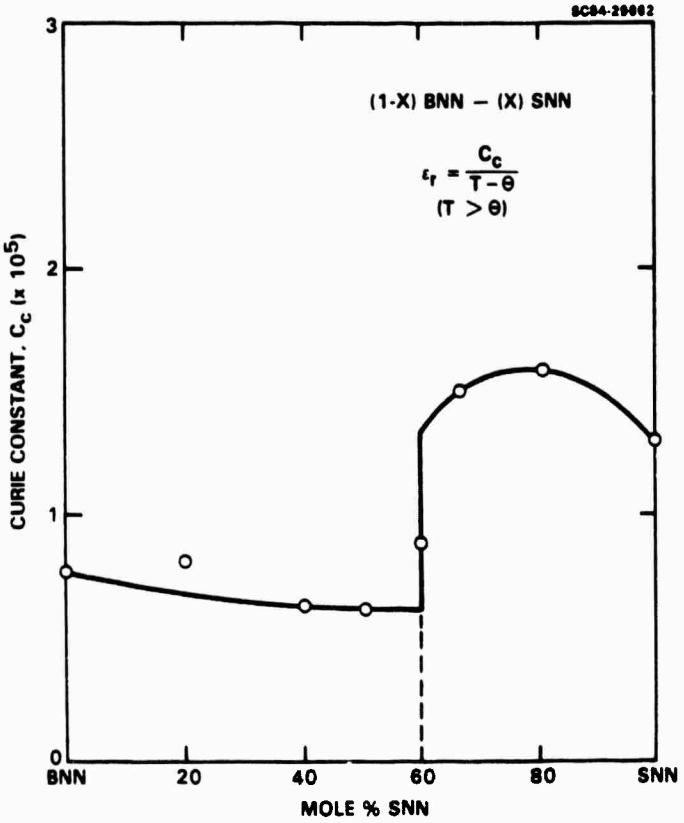

Fig. 8 Curie-Weiss constant vs composition for the system (1-x)BNN-(x)SNN.

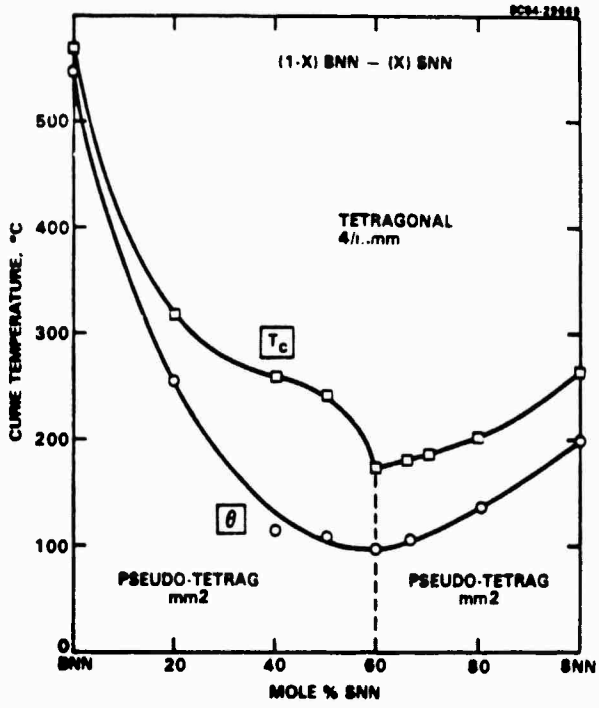

Fig. 9 Curie temperatures T_c, θ vs composition for the system (1-x)BNN-(x)SNN.

These figures help to explain the behavior of the dielectric properties as a function of composition, which are presented in Fig. 10. At the Curie temperature, the dielectric peak is given by

$$\varepsilon_r = \frac{C_c}{T_c - \theta} \quad . \tag{4.1}$$

Since for x near 0.6 there is a strong discontinuity in C_c with only a slowly varying θ, one expects a rather dramatic rise in ε_r for $x > 0.6$, as observed. At room temperature, the dielectric constant is also expected to rise as a result of the T_c minimum and the abrupt jump of the Curie-Weiss coefficient. Hence, the anomalous data point at $x = 0.67$ in Fig. 10, which has been reconfirmed, is in fact expected. Less understood, however, is the apparent sharpness of the room temperature dielectric constant for $0.6 < x < 0.7$. Curiously the paraelectric Curie-Weiss term is only one factor in the full Devonshire dielectric stiffness expansion for $T < \theta$.

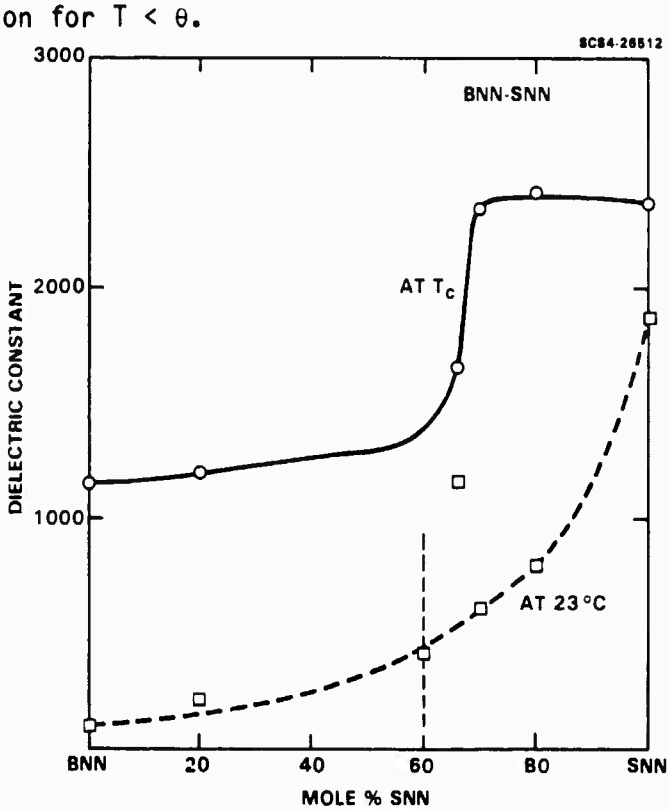

Fig. 10 Dielectric constant at T_c and 23°C vs composition for the system (1-x)BNN-(x)SNN.

The system (1-x)BNN-(x)SNN appears to show morphotropic phase boundary behavior in spite of the fact that both end members are pseudo-tetragonal in form. No measurable increase of the orthorhombic distortion near x = 0.6 appears, but rather an abrupt and simultaneous change of the a and b lattice parameters. This unusual situation for pseudo-binary bronzes perhaps may be due to the ferroelasticity of BNN. Certainly, single crystal growth of near-MPB composition crystals should improve understanding of this interesting system.

4.2 $Pb_2KNb_5O_{15}$-$Ba_2NaNb_5O_{15}$ System

Another tungsten bronze of interest is $Pb_2KNb_5O_{15}$ (PKN). This composition has been grown successfully in hot-pressed ceramic form by Nagata et al[8] in Japan with a high electromechanical coupling constant, k_t = 0.40, and good polarization. As such, it represents an attractive candidate for SAW, piezoelectric and pyroelectric device applications. However, its relatively high Curie point (470°C) makes it very difficult to completely pole. It is also prone to cracking above 1200°C growth temperatures and, hence, to the attainment of optically transparent hot-pressed material.

Because of the orthorhombic structure of PKN, the possibility of obtaining a morphotropic phase composition in combination with pseudo-tetragonal BNN is presented. To this end, we began an investigation of the pseudo binary bronze $(1-x)Pb_2KNb_5O_{15}$-$(x)Ba_2NaNb_5O_{15}$ using cold-pressed and sintered ceramic samples. A morphotropic phase boundary condition was, indeed, found for the composition 0.75 PKN-0.25 BNN, with a sharp minimum in T_c (280°C) and dramatic changes in the dielectric properties near the MPB, as shown in Fig. 11. Again, the Curie-Weiss dielectric behavior of this system helps to shed light on the compositional variation of the dielectric properties. Figure 12 shows the Curie-Weiss coefficient as a function of composition, and C_c varies rapidly up to x = 0.5, with a sharp discontinuity occurring at the MPB.

SC5340.8SA

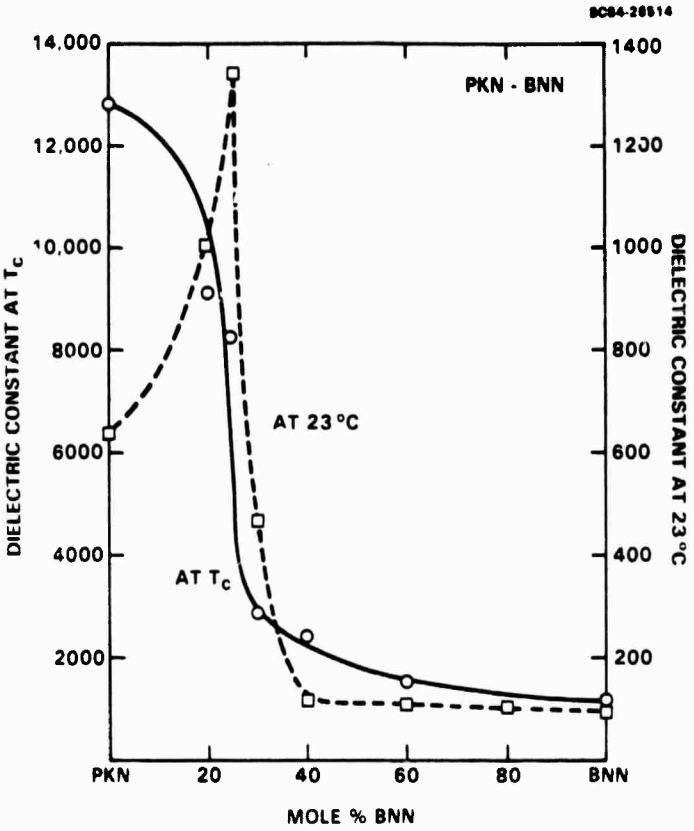

Fig. 11 Dielectric constant at T_C and 23°C vs composition for the system (1-x)PKN-(x)BNN.

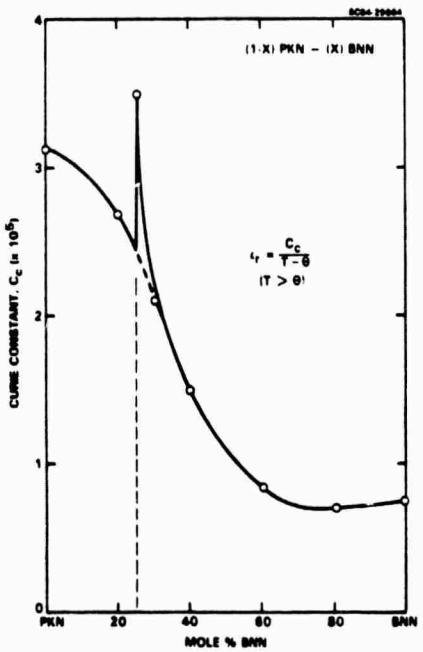

Fig. 12 Curie-Weiss constant vs composition for the system (1-x)PKN-(x)BNN.

The variations of T_c and θ with composition, based on recent and earlier measurements, are shown in Fig. 13. The system shows second order phase transition behavior ($T_c = \theta$) on the orthorhombic (PKN-rich) side of the MPB, and first order behavior on the pseudo-tetragonal side. This second to first order change is largely responsible for the steep decline of the dielectric constant at the Curie temperature, as shown in Fig. 11. The peak in the dielectric constant at room temperature, on the other hand, is due to the rapid decline of T_c and θ on the orthorhombic side of the composition up to the morphotropic phase boundary, followed by a change to first order with a rapid increase of θ and a decrease of C_c. However, due to a tail in the dielectric stiffness characteristics for $T << \theta$ the room temperature dielectric values are all nearly a factor of 2 greater than the predicted values from classical second order transition theory, given by

$$\varepsilon_r = \frac{C_c}{2(\theta - T)} \quad (T < \theta) \quad . \tag{4.2}$$

This behavior is observed over the entire compositional range; an example is given in Fig. 14 for $x = 0.60$.

The PKN-BNN system displays some very strong changes in the dielectric properties at the morphotropic phase boundary. These changes are consistent with the abrupt change in b and c lattice parameters discussed in the last report. As such, compositions near the MPB could be very attractive for both pyroelectric ($x > 0.25$) and electro-optic ($x < 0.25$) applications. Certainly single crystal growth of this material would be desirable, although as a Pb-containing solid solution, Czochralski growth may be difficult. An alternative in this case may be hot-pressed, grain-oriented ceramic densification if single crystal growth proves infeasible.

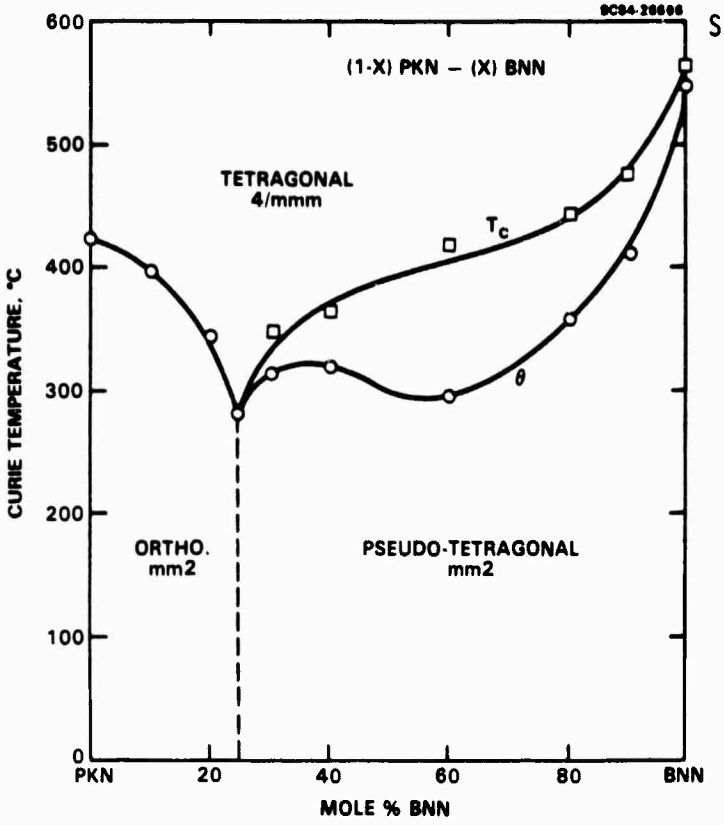

Fig. 13 Curie temperatures T_C, θ vs composition for the system (1-x)PKN-(x)BNN.

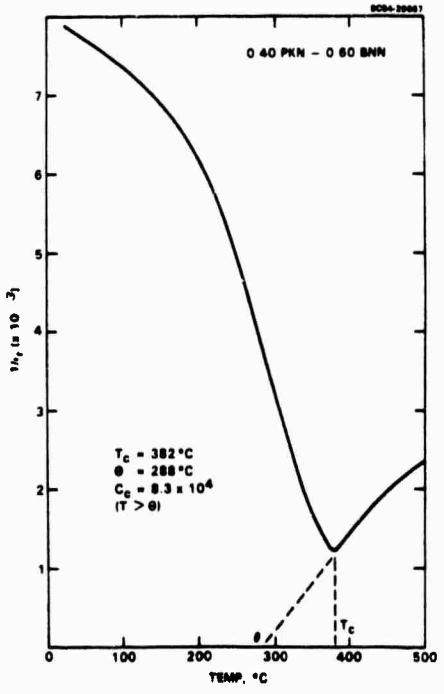

Fig. 14 Reciprocal dielectric properties of 0.40 PKN-0.60 BNN as a function of temperature. Phase transition is first order.

5.0 THERMODYNAMIC PHENOMENOLOGY FOR BRONZE FERROELECTRIC SYSTEMS

5.1 Phenomenology

An empirical thermodynamic elastic Gibbs function that will describe the polarization induced changes in the dielectric, elastic, thermal, piezoelectric and electro-optic properties in all possible simple proper ferroelectric phases of the tungsten bronze structure ferroelectrics can be developed.

Under the symmetry constraints of the 4/mmm point symmetry of the prototype form of the bronzes, the permitted dielectric stiffness α_{ij}, fourth order stiffnesses α_{ijkl}, electrostriction constants Q_{ijkl} elastic compliances s_{ijkl} and sixth order dielectric stiffnesses α_{ijklmn} are listed in Tables 7 through 10.

Table 7

Equivalent Second and Fourth Rank Dielectric Terms for 4/mmm Symmetry

Nye's Matrix Notation		Full Tensor Notation		Number of Equivalent Terms
Term	Symmetry Equivalent Terms	Term	Symmetry Equivalent Terms	
α_1	α_2	α_{11}	α_{22}	2
α_3		α_{33}		1
α_{11}	α_{22}	α_{1111}	α_{2222}	2
α_{12}	α_{21}, α_{66}	α_{1122}	α_{1212}, α_{1221}, α_{2112}, α_{2121}, α_{2211}	
α_{13}	α_{31}, α_{23}, α_{32}, α_{44}, α_{55} ($\alpha_{44} = 4\alpha_{2323}$)	α_{1133}	α_{3311}, α_{2233}, α_{1313}, α_{1313}, α_{1331}, α_{3113}, α_{3131}, α_{2323}, α_{2332}, α_{3223}, α_{3232}	12
α_{33}		α_{3333}		1

Table 8

Equivalent Electrostriction Terms for 4/mmm Symmetry

Nye's Matrix Notation		Full Tensor Notation		Number of Equivalent Terms
Term	Symmetry Equivalent Terms	Term	Symmetry Equivalent Terms	
Q_{11}	Q_{22}	Q_{1111}	Q_{2222}	2
Q_{12}	Q_{21}	Q_{1122}	Q_{2211}	2
Q_{13}	Q_{23}	Q_{1133}	Q_{2233}	2
Q_{31}	Q_{32}	Q_{3311}	Q_{3322}	2
Q_{33}		Q_{3333}		1
Q_{44}	Q_{45}	Q_{2323}	Q_{2332}, Q_{3223}, Q_{3232}, Q_{1313}, Q_{1331}, Q_{8113}, Q_{3151}	8
Q_{66}		Q_{1212}	Q_{1221}, Q_{2112}, Q_{2121}	4

Table 9

Equivalent Elastic Compliance Terms for 4/mm Symmetry

Nye's Matrix Notation		Full Tensor Notation		Number of Equivalent Terms
Term	Symmetry Equivalent Terms	Term	Symmetry Equivalent Terms	
s_{11}	s_{22}	s_{1111}	s_{2222}	2
s_{12}	s_{21}	s_{1122}	s_{2211}	2
s_{13}	s , s_{23}, s_{32}	s_{1133}	s_{3311}, s_{2233}, s_{3322}	4
s_{33}		s_{3333}		1
s_{44}	s_{55}	s_{2323}	s_{2332}, s_{3223}, s_{3232}, s_{1313}, s_{1331}, s_{3113}, s_{3131}	8
s_{66}		s_{1212}	s_{1221}, s_{2112}, s_{2121}	4

Table 10

Equivalent Sixth Rank Tensor Terms of the Form $\alpha(P^6)$ for 4/mm Symmetry

	Term	Symmetry Related Terms	Number of Equivalent Terms
1.	α_{111}	222	2
2.	α_{112}	166, 121, 616, 661, 211, 221, 266, 212, 626, 662, 122	30
3.	α_{113}	155, 131, 515, 551, 331, 223, 244, 232, 424, 442, 322	30
4.	α_{123}	144, 132, 525, 645, 546, 636, 663, 564, 654, 552, 321, 441, 231, 465, 366, 255, 456, 213, 414, 312	90
5.	α_{133}	535, 553, 331, 355, 313, 233, 434, 443, 332, 344, 323	30
6.	α_{333}		1

Using the reduced notation 11 → 1, 22 → 2, 33 → 3, 23 or 32 → 4, 13 or 31 → 5 and 12 or 21 → 6 the elastic Gibbs function takes the form

$$\begin{aligned}\Delta G_1 = {} & \alpha_1(P_1^2 + P_2^2) + \alpha_3 P_3^2 + \alpha_{11}(P_1^4 + P_2^4) + \alpha_{33}P_3^4 \\ & + \alpha_{13}(P_1^2P_3^2 + P_2^2P_3^2) + \alpha_{12}P_1^2P_2^2 + \alpha_{333}P_3^6 \\ & + \alpha_{111}(P_1^6 + P_2^6) - \tfrac{1}{2}s_{11}(X_1^2 + X_2^2) - s_{12}X_1X_2 \\ & - s_{13}(X_1 + X_2)X_3 - \tfrac{1}{2}s_{33}X_3^2 - \tfrac{1}{2}s_{44}(X_4^2 + X_5^2) \\ & - \tfrac{1}{2}s_{66}S_6^2 - Q_{11}(P_1^2X_1 + P_2^2X_2) - Q_{12}(P_1^2X_2 + P_2^2X_1) \\ & - Q_{13}(P_1^2X_3 + P_2^2X_3) - Q_{31}(P_3^2X_1 + P_3^2X_2) \\ & - Q_{33}P_3^2X_3 - Q_{44}(P_2P_3X_4 + P_1P_3X_5) \\ & - Q_{66}P_1P_2X_6 \end{aligned} \qquad (5.1)$$

The first partial derivatives with respect to the polarization give the field components

$$\frac{\partial \Delta G}{\partial P_1} = E_1 = 2\alpha_1 P_1 + 4\alpha_{11} P_1^3 + 2\alpha_{13} P_1 P_3^2 + 2\alpha_{12} P_1 P_2^2 + 6\alpha_{111} P_1^5 + Q_{13} P_1 X_3 + Q_{44} P_3 X_5 + Q_{66} P_1 X_6 \tag{5.2}$$

$$\frac{\partial \Delta G}{\partial P_2} = E_2 = 2\alpha_1 P_2 + 4\alpha_{11} P_2^3 + 2\alpha_{13} P_2 P_3^2 + 2\alpha_{12} P_2 P_1^2 + 6\alpha_{111} P_2^5 + 2Q_{13} P_2 X_3 + Q_{44} P_3 X_4 + Q_{66} P_1 X_6 \tag{5.3}$$

$$\frac{\partial \Delta G}{\partial P_3} = E_3 = 2\alpha_3 P_3 + 4\alpha_{33} P_3^3 + 2\alpha_{13}(P_1^2 + P_2^2) P_3 + 6\alpha_{33} P_3^5 + 2Q_{31} P_3 (X_1 + X_2) + 2Q_{33} P_3 X_3 + Q_{44}(P_2 X_4 + P_1 X_5) \tag{5.4}$$

The solutions of these equations with $E_i = 0$ determine the ferroelectric states for a free crystal ($X = 0$). In general, seven possible ferroelectric species can occur from the prototypic 4/mmm symmetry of the paraelectric phase of the tungsten bronze, each of which corresponds to a different combination of nonzero (spontaneous) values of the P_i components. All possible solutions for the three Eqs. (5.2)-(5.4) were derived and reported by Cross and Pohanka (1968).

Practically, however, just two of these solutions encompass all presently known simple ferroelectric bronzes. They are

$$\text{(a)} \quad P_3^2 \neq 0 \qquad P_1 = P_2 = 0$$

$$\text{(b)} \quad P_1^2 = P_2^2 \neq 0 \qquad P_3 = 0 \quad .$$

The species (a) corresponds to the Shuvalov (1970) species 4/mmm (1) D4 F4mm where 4/mmm is the high temperature prototype point group and F4mm means that the crystal is ferroelectric of point group 4mm below the transition temperature. D4 indicates that the spontaneous polarization P_s has definite orientations along the four-fold symmetry axes, and (1) denotes the number of equivalent four-fold axis, which is one. In other words, two domains of opposite orientation of P_s (i.e., 180° domains) are along the four-fold prototypic axis. The second species (b) is one of the subtypes of 4/mmm (2)D2 Fmm2 with P_s along the two-fold axis which make angles of 45° with the 1 and 2 prototype axis ($P_1^2 = P_2^2$) and has four equivalent ferroelectric domain states.

Substituting the conditions (a) into the general Eqs. (5.2)-(5.4) gives the following conditions for stability:

$$P_1 = P_2 = 0 \qquad 0 = 2\alpha_3 + 4\alpha_{33}P_3^2 + 6\alpha_{333}P_3^4 \qquad (5.5)$$

The isothermal dielectric stiffnesses χ_{ij} are

$$\chi_{11}^T = 2\alpha_1 + 2\alpha_{13}P_3^2$$

$$\chi_{22}^T = 2\alpha_1 + 2\alpha_{13}P_3^2$$

$$\chi_{33}^T = 2\alpha_3 + 12\alpha_{33}P_3^2 + 30\alpha_{333}P_3^4$$

$$\chi_{12}^T = \chi_{13}^T = \chi_{23}^T = 0 \quad . \tag{5.6}$$

The tetragonal spontaneous strains are given by

$$x_1 = Q_{31}P_3^2 \qquad x_4 = x_5 + x_6 = 0$$

$$x_2 = Q_{31}P_3^2$$

$$x_3 = Q_{33}P_3^2 \quad , \tag{5.7}$$

and the piezoelectric b coefficients by

$$b_{11} = 0 \qquad b_{21} = 0 \qquad b_{31} = 2Q_{31}P_3$$

$$b_{12} = 0 \qquad b_{22} = 0 \qquad b_{32} = 2Q_{31}P_3$$

$$b_{13} = 0 \qquad b_{23} = 0 \qquad b_{33} = 2Q_{33}P_3$$

$$b_{14} = 0 \qquad b_{24} = Q_{44}P_3 \qquad b_{34} = 0$$

$$b_{15} = Q_{44}P_3 \qquad b_{25} = 0 \qquad b_{35} = 0$$

$$b_{16} = 0 \qquad b_{26} = 0 \qquad b_{36} = 0 \quad . \tag{5.8}$$

For the case (b), the corresponding equations take the form for the stability conditions given by

$$P_1^2 = P_2^2 \qquad 0 = 2\alpha_1 + (4\alpha_{11} + 2\alpha_{12})P_1^2 + 6\alpha_{111}P_1^4$$

$$P_3 = 0 \quad . \tag{5.9}$$

In this case the isothermal stiffnesses are

$$\chi_{11}^T = 2a_1 + 12\alpha_{11}P_1^2 + 2\alpha_{12}P_1^2 + 30\alpha_{111}P_1^4$$

$$\chi_{22}^T = 2\alpha_1 + 12\alpha_{11}P_1^2 + 2\alpha_{12}P_1^2 + 30\alpha_{111}P_1^4$$

$$\chi_{33}^T = 2\alpha_3 + 4\alpha_{13}P_1^2$$

$$\chi_{34}^T = 4\alpha_{12}P_1^2 \qquad \chi_{13} = \chi_{23} = 0 \quad . \tag{5.10}$$

It should be noted that the coefficients here are expressed with respect to the original prototypic axes and thus satisfy pseudo-monoclinic symmetry. However, a simple rotation of the matrix by 45° in the 1,2 plane would reveal the true orthorhombic symmetry.

The spontaneous elastic strains take the form

$$x_1 = (Q_{11} + Q_{12})P_1^2$$

$$x_2 = (Q_{11} + Q_{12})P_1^2$$

$$x_3 = 2Q_{13}P_1^2$$

$$x_6 = Q_{66}P_1^2 \qquad x_4 = x_5 = 0 \quad , \tag{5.11}$$

and the piezoelectric coefficients are

$$b_{11} = 2Q_{11}P_1 \qquad b_{21} = 2Q_{12}P_1 \qquad b_{31} = 0$$

$$b_{12} = 2Q_{12}P_1 \qquad b_{22} = 2Q_{11}P_1 \qquad b_{32} = 0$$

$$b_{13} = 2Q_{13}P_1 \qquad b_{23} = 2Q_{13}P_1 \qquad b_{33} = 0$$

$$b_{14} = 0 \qquad b_{24} = 0 \qquad b_{34} = Q_{44}P_1$$

$$b_{15} = 0 \qquad b_{25} = 0 \qquad b_{35} = Q_{44}P_1$$

$$b_{16} = Q_{66}P_1 \qquad b_{26} = Q_{66}P_1 \qquad b_{36} = 0 \quad . \qquad (5.12)$$

5.2 Potential Utility of the Phenomenological Theory

5.2.1 Introduction

Tables 7 through 10 show the substantial number of constants required to characterize the bronzes in this phenomenological manner. The only formal benefit is that all the elasto-dielectric parameters of the lower symmetry ferroelectric forms can be characterized in terms of the nonlinear parameters of the higher symmetry prototype form.

In principle, possibly all the parameters can be functions of both temperature and composition. However, both direct and indirect evidence suggests that:

(a) The dominant temperature dependence is carried in the terms α_1 and α_3 which have a Curie Weiss form

$$\alpha_1 = \alpha_{10} (T - \theta_1)$$

$$\alpha_3 = \alpha_{30} (T - \theta_3) \quad .$$

(b) The higher order constants do not change markedly with either temperature or composition across a wide field of compounds and solid solutions with bronze structure.

In earlier studies we have demonstrated that:

(1) In all known ferroelectric bronzes, only two of the seven possible ferroelectric species that are available from the 4/mmm prototype occur in nature.

(2) In the tetragonal ferroelectric form in $(Sr_{0.61}Ba_{0.39})Nb_2O_6$, which is the congruently melting SBN composition, the data follow very closely to the phenomenology except for temperatures close to the Curie point T_c, and all parameters have been evaluated.

(3) For $(Pb_{1-x}Ba_x)Nb_2O_6$ in the tetragonal phase field close to the morphotropic phase boundary at the $(Pb_{0.6}Ba_{0.4})Nb_2O_6$ composition, the dielectric, piezoelectric and electro-optic behavior can be modeled quite accurately using the phenomenological constants for SBN and adjusting θ_1 and θ_3 to conform to the observed Curie Weiss behavior.

The success to data with modeling suggests that we attempt a more ambitious assessment of the range of validity of our simple hypotheses (a) and (b) above, using a much wider range of bronze compounds, and making use of literature values to evaluate directly, wherever possible, the stiffness parameters.

5.2.2 Evaluation of the Thermodynamic Parameters

More than 100 different ferroelectric compounds with the tungsten bronze structure have been synthesized, and innumerable solid solutions can be made between these end member compositions. However, reliable experimental data from which to evaluate the thermodynamic constants is lacking. For many materials, only ceramic samples have been made, and for the separation of the individual tensor components is impossible. Even in many systems where good single crystals have been grown, the headlong rush to print has left many of the important parameters unmeasured.

For this study we have found adequate but incomplete data for several $Sr_{1-x}Ba_xNb_2O_6$ (SBN) solid solutions. In several La_2O_3:$Sr_2KNb_5O_{15}$ compounds and solid solutions and for pure $Sr_2KNb_5O_{15}$, the data are also adequate, though incomplete. $Ba_2NaNb_5O_{15}$ may be analyzed with this model if the weak ferroelastic phase change near 370°C is neglected, and there are also some data for titanium modified $Ba_2NaNb_5O_{15}$. Similarly, in $K_3Li_2Nb_5O_{15}$ adequate data for some of the constants were found, although the transverse dielectric response apparently has not been measured.

In the orthorhombic ferroelectric form, we have been able to find data only for $PbNb_2O_6$ and for $Pb_2KNb_5O_{15}$. The fitting to obtain the thermodynamic parameters is, however, more difficult for these compositions and will be covered in a subsequent report. For the tetragonal ferroelectric form, the evaluation is relatively straightforward. The constant α_3 has the form $\alpha_3 = \alpha_{30}(T - \theta_3)$ which leads to an equation for the stiffness χ_{33} above T_c of the form

$$\chi_{33} = 2\alpha_{30}(T - \theta_3) \qquad (T > \theta_3) \tag{5.13}$$

Thus the extrapolation of the Curie-Weiss plot of stiffness above T_c gives the temperature θ, and from the slope, the constant $2\alpha_{30}$.

By equating the ΔG values in ferroelectric and paraelectric states at T_c, the equation for P_s (Eq. (5.5)) can be put into the Devonshire form

$$\frac{T - \theta}{T_c - \theta} - 4\left(\frac{P_3}{P_{30}}\right)^2 + 3\left(\frac{P_3}{P_{30}}\right)^4 = 0 \quad , \tag{5.14}$$

in which $T_c - \theta$ and P_{30} are the only fitting parameters. Unfortunately, the published P_s vs T data for ferroelectric crystals is often unreliable, particularly at temperatures remote from T_c where it is difficult to pole to a single domain state. Thus, we suggest checking the shape of the polarization function by using a less direct method. For example, the spontaneous strains $\Delta c/c$ and $\Delta a/a$ induced in the ferroelectric form are electrostrictive in nature and thus scale with P_s^2. Similarly, the optical impermeability changes below T_c (ΔB_{11} and Δb_{33}) are quadratic and scale with P_s^2. The piezoelectric b_{ij} constants, on the other hand, are morphic and scale directly with P_s, as do the linear electro-optic and the nonlinear Miller δ coefficients.

Typical fitting of the different P_s data for $Ba_2NaNb_2O_6$ is shown in Fig. 15. Clearly the Devonshire form is in excellent agreement with the birefringence data, which are probably more reliable in this crystal. From the values of T_c, θ, P_{so} and α_{30}, the α constants are given by

$$\alpha_3 = 1/2\ \alpha_{30}(T_c - \theta_3)$$

$$\alpha_{33} = -\frac{\alpha_{30}(T_c - \theta_3)}{P_{so}}$$

$$\alpha_{333} = \frac{\alpha_{30}(T_c - \theta_3)}{2(P_{so})^4} \quad . \tag{5.15}$$

For the constants α_{10} and α_{13}, dielectric data for a section parallel to the a axis (ε_a) are required. Above T_c,

$$\chi_1 = 2\alpha_{10}(T - \theta_1) \quad , \tag{5.16}$$

so that $2\alpha_{10}$ is the Curie-Weiss slope and θ_1 is the extrapolated Curie temperature. To derive α_{13}, Eq. (5.6) can be used to obtain, by least-squares method, a best fit to the experimental data below T_c, taking now calculated values for P_3 vs T. A typical plot comparing measured and calculated values for $Ba_2NaNb_5O_{15}$ is given in Fig. 16.

Table 11 lists derived constants for the bronze compositions using these methods. For α_{30} and α_{333} excellent agreement over a broad selection of bronze compositions may be noted. The values for α_{10} also agree within a narrow range, though here the stiffness is much larger and the Curie-Weiss slope is more difficult to read precisely. The α_{33} values cover a wider range, which perhaps is not surprising, since in the elastic Gibbs function, the negative value of α_{33} occurs because of a strong contribution from elastic and electrostrictive constants in the free crystal. Thus, the magnitude of α_{33} is markedly dependent on the elastic boundary conditions and probably therefore on the crystal perfection. The α_{13} values also cover a rather wide range, but here the error is probably more in the evaluation.

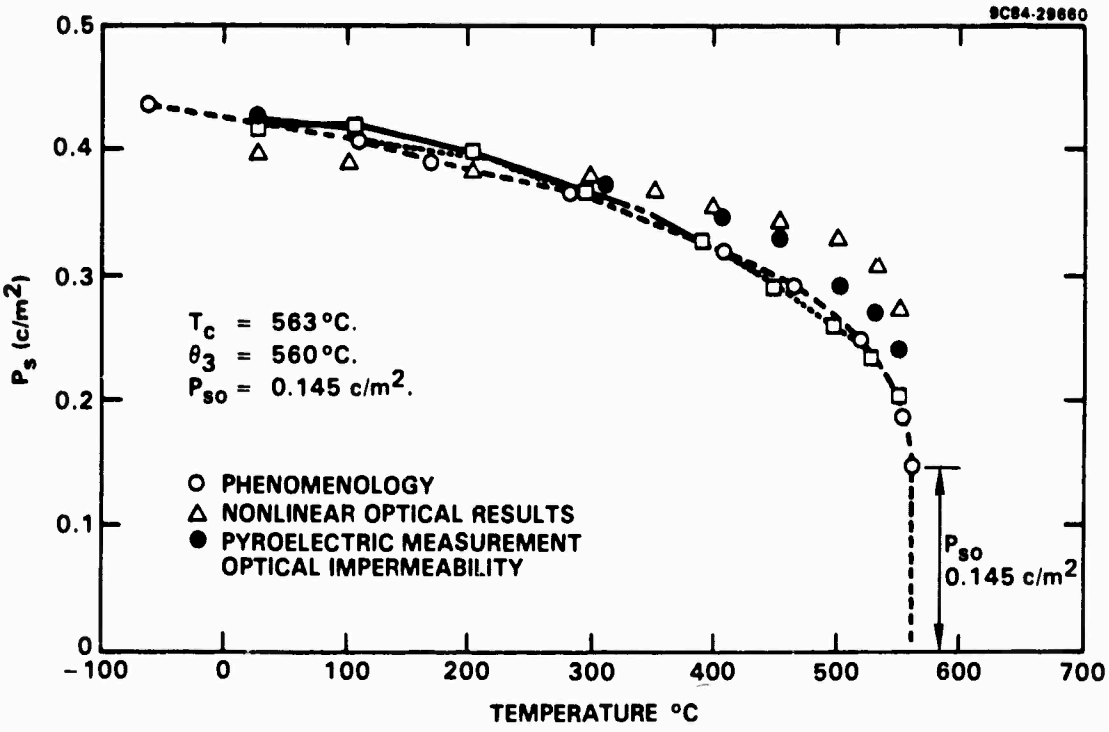

Fig. 15 Phenomenological fitting of P_s vs T for $Ba_2NaNb_5O_{15}$. T_c = 563°C, θ_3 = 560°C, P_{so} = 0.145 c/m^2.

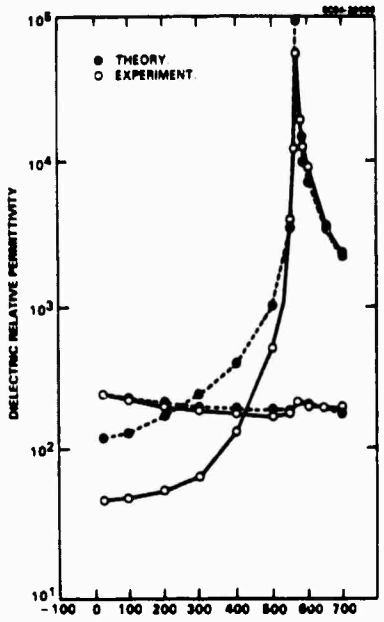

Fig. 16 Phenomenological fitting to the dielectric permittivity for single crystal $Ba_2NaNb_5O_{15}$.

Table 11

Thermodynamic Constants for Tetragonal Tungsten Bronze Ferroelectric Crystals

Compound	1/2 α_{30}	12 α_{33}	30 α_{333}	1/2 α_{10}	α_{13}
$Sr_{0.25}Ba_{0.75}Nb_2O_6$	$2.4\ 10^{-6}$	$-2.3\ 10^{-3}$	$3.6\ 10^{-1}$		
$Sr_{0.5}Ba_{0.5}Nb_2O_6$	$2.4\ 10^{-6}$	$-6.2\ 10^{-3}$	$3.2\ 10^{-1}$		
$Sr_{0.6}Ba_{0.4}Nb_2O_6$	$1.6\ 10^{-6}$	$-11.0\ 10^{-3}$	$3.6\ 10^{-1}$		
$SR_{0.67}Ba_{0.33}Nb_2O_6$	$2.7\ 10^{-6}$	$-1.6\ 10^{-3}$	$3.1\ 10^{-1}$		
$Sr_{0.61}Ba_{0.39}Nb_2O_6$	$2.52\ 10^{-6}$	$-8.4\ 10^{-3}$	$3.6\ 10^{-1}$	$3.73\ 10^{-6}$	$2.1\ 10^{-3}$
$KSr_2Nb_5O_{15}$	$3.45\ 10^{-6}$	$-9.7\ 10^{-3}$	$3.4\ 10^{-1}$	$2.4\ 10^{-6}$	$11.3\ 10^{-3}$
3% (La) $Sr_2KNb_5O_{15}$	$2.2\ 10^{-6}$	$-9.6\ 10^{-3}$	$2.85\ 10^{-1}$		
6% (La) $Sr_2KNb_5O_{15}$	$2.0\ 10^{-6}$	$-10.5\ 10^{-3}$	$3.8\ 10^{-1}$		
9% (La) $Sr_2KNb_5O_{15}$	$3.14\ 10^{-6}$	$-12.2\ 10^{-3}$	$3.58\ 10^{-1}$		
$Ba_2NaNb_5O_{15}$	$3.44\ 10^{-6}$	$-11.46\ 10^{-3}$	$2.5\ 10^{-1}$	$5.15\ 10^{-6}$	$13.3\ 10^{-3}$
$Ba_{4.65}Na_{1.65}Nb_{9.65}Ti_{0.35}O_{30}$	$3.56\ 10^{-6}$	$-5.34\ 10^{-3}$	$1.63\ 10^{-1}$		
$K_3Li_2Nb_5O_{15}$	$2.87\ 10^{-6}$	$-14.16\ 10^{-3}$	$1.13\ 10^{-1}$	$2.82\ 10^{-6}$	

In summary, these preliminary data appear to confirm that the original hypothesis of a constancy of the higher order stiffnesses is a good approximation for tetragonal bronze ferroelectrics, and thus can form a basis for the analysis of the properties of a very wide range of bronze compositions.

6.0 APPLICATION OF THE BAND TRANSPORT MODEL TO PHOTOREFRACTIVE SBN:60

6.1 Introduction

The effectiveness of strontium barium niobate (SBN) as a photorefractive material has been shown to increase with the addition of certain dopants.[9,10] In particular, work at Caltech has demonstrated that the introduction of cerium into SBN results in a crystal with a significantly larger two-beam coupling coefficient, but with a similar speed of response.[10] To explain these results and, thereby, to propose new ideas for increasing the speed of SBN, a charge transport model for SBN needs to be presented. Although both the hopping model[11] and the band transport model[12,13] describe charge transport in photorefractive materials, only the latter will be analyzed here.

6.2 Band Transport Theory

The band transport model assumes that electrons (or holes) are optically excited from filled donor (or acceptor) sites to the conduction (or valence) band where they migrate to dark regions in the crystal by drift or diffusion before recombining into an empty trap. The transported charge results in a space charge grating that in general, is out of phase with the incident irradiance (Fig. 17). A space charge electric field develops to balance the space charge grating in accordance with Poisson's equation, and this space charge field modulates the refractive index.

A mathematical description of the grating formation process is given by the equations developed most fully by Kukhtarev[12-14] and co-workers:

$$\frac{\partial n}{\partial t} - \frac{\partial N_D^+}{\partial t} = \frac{1}{e}\frac{\partial J}{\partial z} \text{ (continuity)} \quad , \tag{6.1}$$

$$\frac{\partial N_D^+}{\partial t} = \frac{sI}{h\nu}(N_D - N_D^+) - \gamma_R n N_D^+ \text{ (rate equation)} \quad , \tag{6.2}$$

$$J = e\mu nE - k_B T\mu \frac{\partial n}{\partial z} \text{ (current equation)} \quad , \tag{6.3}$$

$$\frac{\partial E}{\partial z} = \frac{e}{\varepsilon}\,(n + N_A - N_D^+) \quad \text{(Poisson's equation)} \tag{6.4}$$

where

n = electron number density

N_D = total number density of dopants

N_D^+ = number density of ionized donors

N_A = number density of empty traps under dark conditions

(Note: $(N_D^+(I=0) = N_A)$

$N_D - N_D^+$ = number density of donors

J = current density

s = photoionization cross section

I = irradiance

ν = frequency of light used

γ_R = two-body recombination rate

μ = mobility

E = total electric field

k_B = Boltzmann's constant

T = temperature

e = charge on the electron

ε = static dielectric constant

h = Planck's constant.

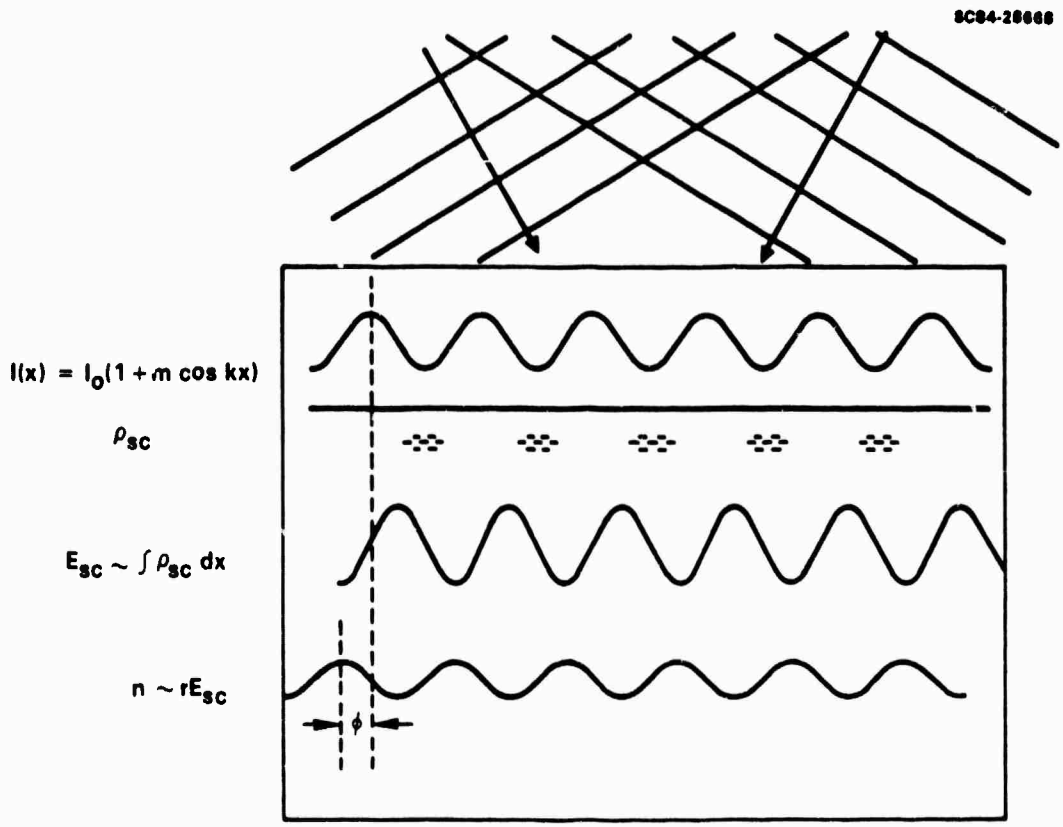

Fig. 17 The photorefractive mechanism.

Equations (6.1)-(6.4) neglect dark conductivity and the bulk photovoltaic effect. These equations also do not consider secondary trapping levels or photorefractive centers. In Eq. (6.2) the optical irradiance I is assumed to be of the form

$$I = I_0(1 + m \cos k_g z) \quad , \tag{6.5}$$

where m is the modulation index, k_g is the grating wave number, and I_0 is the average irradiance.

Equations (6.1)-(6.5) must be supplemented with an electro-optic relation between the space charge field and the change in the crystal refractive index, Δn. Thus,

$$\Delta n = \frac{1}{2} n_b^3 r_{eff} \delta E \quad , \tag{6.6}$$

where δE is the spatially varying component of E, n_b is the background refractive index and r_{eff} is the effective electro-optic coefficient.

Equations (6.1)-(6.6) can be solved with two approximations: linearization in the grating modulation index and the zeroth-order approximation in the electron number density, n_o.[14] Using these we obtain the two-beam coupling coefficient, Γ, given by

$$\Gamma = \mathrm{Re}\left\{ i \frac{\omega}{c} n_1 e^{-i\phi_1} \right\} \tag{6.7}$$

where

$$n_1 = \frac{1}{2} n_b^3 r_{eff} E_{sc} \quad ,$$

$$E_{sc} = E_q \left[\frac{E_o^2 + E_D^2}{E_o^2 + (E_D + E_q)^2} \right]^{1/2} \quad .$$

E_o = applied field (normal to grating planes) ,

$$E_D = \frac{k_B T k_g}{e} \quad ,$$

$$E_q = \frac{eN_A}{\epsilon k_g} \frac{1}{1 + N_A/(N_D - N_A)} \quad ,$$

and

$$\tan \phi_1 = \frac{E_D}{E_o}\left[1 + \frac{E_D}{E_q} + \frac{E_o^2}{E_D E_q}\right] .$$

The transient response has an overdamped oscillatory behavior with a response time τ_e given by

$$\tau_e = \tau_{di} \frac{(1 + \tau_R/\tau_D)^2 + (\tau_R/\tau_E)^2}{[1 + \tau_R \tau_{di}/(\tau_D \tau_I)]\,(1 + \tau_R/\tau_D) + (\tau_R/\tau_E)^2(\tau_{di}/\tau_I)} \qquad (6.8)$$

where

$$\tau_{di} = \frac{\varepsilon}{e\mu n_o} \text{ (dielectric relaxation time)} ,$$

$$\tau_E = \frac{1}{k_g \mu E_o} \text{ (drift time)} ,$$

$$\tau_D = \frac{e}{\mu k_B T k_g^2} \text{ (diffusion time)} ,$$

$$\tau_R = \frac{1}{\gamma_R N_A} \text{ (recombination time)} ,$$

$$\tau_1 = \frac{1}{sI_o/(h\nu) + \gamma_R n_o} ,$$

with the zeroth-order electron number density given by

$$n_o = \frac{sI_o(N_D - N_A)}{h\nu\gamma_R N_A} .$$

6.3 Results for SBN:60

In order to apply this model to SBN:60, several material parameters need to be specified. The relative dielectric constant, the electro-optic coefficient, and the background refractive index are readily available; ε_{33} = 930, r_{33} = 400 pm/V, and n_e = 2.3. However, the mobility, the two-body recombination rate, the photoionization cross section and the dopant number density are not known specifically for SBN. Since $BaTiO_3$ is also a highly electro-optic, ferroelectric and photorefractive material, the mobility and the two-body recombination rate coefficient for SBN will be estimated by data given for $BaTiO_3$, specifically μ = 0.5 cm^2/Vs and $\lambda_R = 5 \times 10^{-8}$ cm^3/s.[11,15] For SBN doped with Ce (0.1 percent by weight), the dopant number density will be on the order of 10^{19} cm^{-3}. The photoionization cross section can be obtained from absorption coefficient measurements through the relation $\alpha = s(N_D - N_A) \approx sN_D = 1.8$ cm^{-1},[10] since, usually, $N_D << N_A$; hence, $s \approx 1.8 \times 10^{-19}$ cm^2.

The last few parameters to quantify are those which are extrinsically defined. Our experimental apparatus at Caltech is characterized by the following: E_0 = 0 V/cm, T = 298K, I_0 = 1 W/cm^2, λ = 0.5145 μm, and Λ = 5 μm, where λ and Λ are the optical and grating wavelengths, respectively. Therefore, only the density of empty traps under dark conditions, N_A, is defined and it is treated as a variable with the restriction $N_A < N_D$. Figures 18 and 19, then, show the two-beam coupling coefficient Γ and τ_e as a function of N_A.

Experimentally, we have measured $\Gamma \approx 11$ cm^{-1} and $\tau_e \approx 0.10$ s (at 1 W/cm^2) in SBN:Ce[10] which, from Figs. 18 and 19, corresponds to $N_A \approx 1 \times 10^{16}$ cm^{-3}. In undoped SBN, $\Gamma \approx 2$ cm^{-1} and $\tau_e \approx 0.12$ s (at 1 W/cm^2). Therefore, in the as-grown samples, only the two-beam coupling coefficient is significantly affected by the introduction of Ce into SBN.

Equations (6.7) and (6.8) provide a possible explanation for the above experimental results. A similar τ_e implies that the reduction ratio $R = (N_D - N_A)/N_A$ is essentially the same for both crystals. Since the two samples were grown in similar atmospheres with similar partial pressures of oxygen, this argument appears reasonable. The difference in Γ can be attributed to different values of N_A in the two crystals. The plausibility of this suggestion

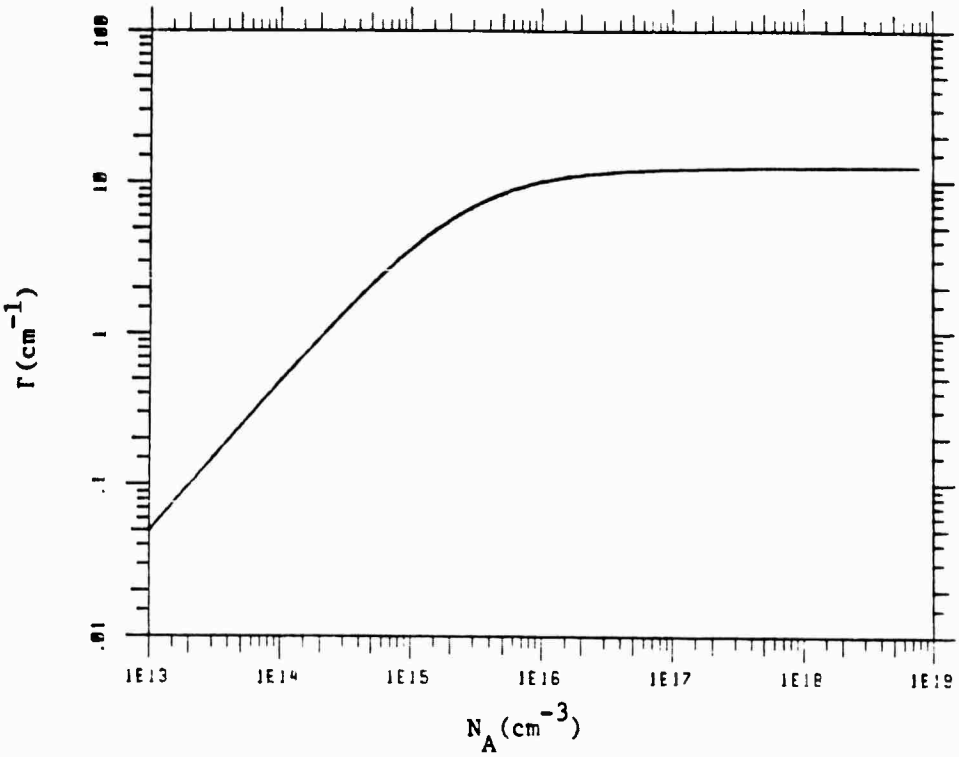

Fig. 18 Two-beam coupling coefficient of SBN:Ce as a function of the trap number density under dark conditions.

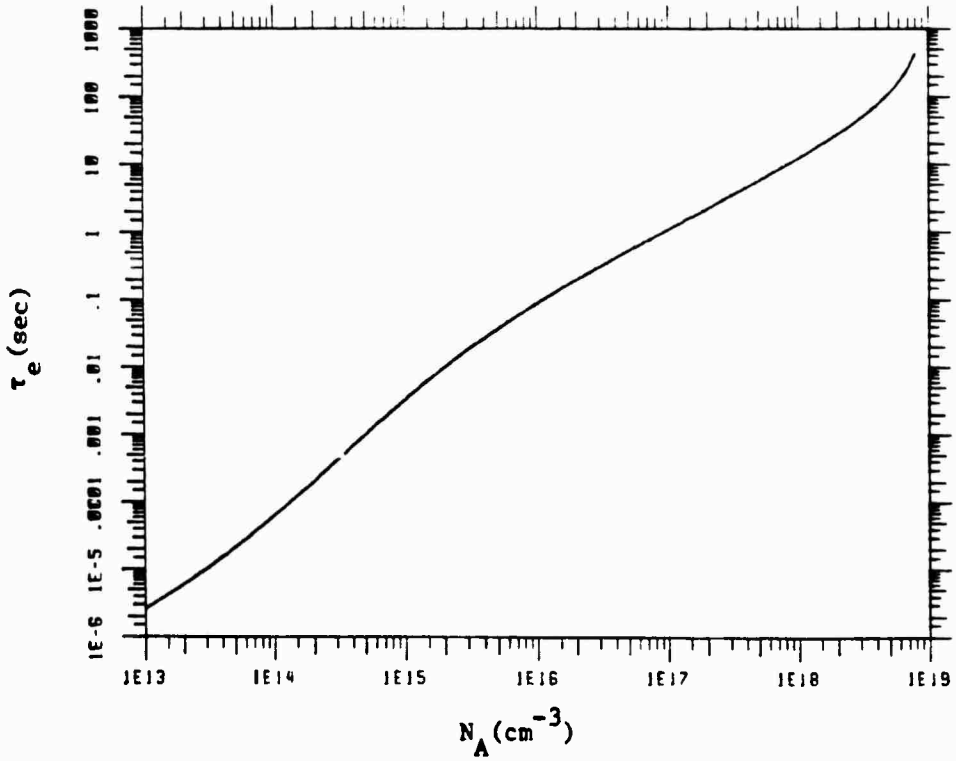

Fig. 19 Response time of SBN:Ce as a function of the trap number density under dark conditions.

rests on the fact that cerium in SBN can be present in two valence states, Ce^{3+} and Ce^{4+}, with Ce^{4+} acting as an acceptor. Then undoubtedly the introduction of Ce into SBN will then undoubtedly increase the number density of Ce^{4+}, which increases N_A and, therefore, the two-beam coupling coefficient.

If the above theory and explanations are indeed valid, then Figs. 18 and 19 indicate that by decreasing N_A in SBN:Ce from 1×10^{16} cm^{-3} to 5×10^{14} cm^{-3}, the two-beam coupling coefficient will reduce to the value observed in undoped SBN, but the response time will now be 1 ms.

In principle, N_A can be decreased easily by heating the sample in an oxygen-deficient atmosphere which will convert Ce^{4+} to Ce^{3+} by extraction of oxygen from the crystal. However, in practice, this process may not necessarily occur. The above all assume that only one photorefractive species exists; Ce was thought to provide Ce^{3+} as the donor and Ce^{4+} as the trap. In fact, crystalline point defects and niobium ions may also contribute to the photorefractive effect in these crystals. Therefore, the proposed heat treatment may not convert Ce^{4+} to Ce^{3+}, but instead it may perturb the balance of the other species. Therefore, a spectroscopic analysis of SBN:Ce both before and after reduction will be needed to determine heat treatment effects.

In conclusion, we have observed and measured the photorefractive effect in optically excellent samples of SBN and SBN:Ce. Band transport theory has been applied successfully to SBN:Ce, and indicates that $N_A \simeq 10^{16}$ cm^{-3} in this sample. An explanation for the increase in the two-beam coupling coefficient in SBN:Ce over that observed in undoped SBN has been proposed, and heat treatment of SBN:Ce in an oxygen deficient atmosphere is suggested as a means of producing a sample with a coupling coefficient $\Gamma \simeq 2$ cm^{-1} and a response time $\tau_e \simeq 1$ ms.

7.0 FUTURE PLANNED WORK

- Further refine and evaluate the growth of high purity SBN:50 and SBN:60 single crystals.

- Continue development of Fe- and Ce-doped SBN:60, and attempt to establish the dopant valence states and the presence, if any, of Nb^{4+}.

- Investigate the dielectric and optical properties of SBN:60 doped with other cations such as Tb^{3+}/Tb^{4+}, Eu^{2+}/Eu^{3+}. Also, investigate the effects of partial reduction on photorefractive speed and sensitivity.

- Establish SBN:50 LPE growth from the SrO-BaO-Nb_2O_5-V_2O_5 flux system.

- Continue development of the BaV_2O_6-PBN:60 and $Pb_{1-x}Ba_xV_2O_6$-PBN:60 flux systems for LPE growth.

- Attempt single crystal growth of near-morphotropic BNN-SNN and PKN-BNN bronze compositions for dielectric, structural and optical evaluation.

- Continue measurement of the E-O coefficients of near-morphotropic single crystal PBN.

8.0 PUBLICATIONS AND PRESENTATIONS

8.1 Publications

1. R.R. Neurgaonkar, W.K. Cory and J.R. Oliver, "Growth and Applications of Ferroelectric Tungsten Bronze Family Crystals," Ferroelectrics 51, 3 (1983).

2. R.R. Neurgaonkar, J.R. Oliver and L.E. Cross, "Ferroelectric Properties of Tetragonal Tungsten Bronze Single Crystals," Ferroelectrics 56, 31 (1984).

3. T.R. Shrout, L.E. Cross and D.A. Hukin, "Ferroelectric Properties of Tungsten Bronze Lead Barium Niobate (PBN) Single Crystals."

8.2 Presentations

1. R.R. Neurgaonkar, W.K. Cory and J.R. Oliver, "Growth and Applications of Tungsten Bronze Family Crystals," presented at the 1983 IEEE Int. Symp. on Applications of Ferroelectrics, June 1-3, 1983, Gaithersburg, MD.

2. R.R. Neurgaonkar, J.R. Oliver and L.E. Cross, "Growth and Application of Ferroelectric Tungsten Bronze Family Crystals," presented at the 5th European Meeting on Ferroelectrics, Sept. 26-30, 1983, Benalmadena, Spain.

3. T.R. Shrout, H.C. Chen and L.E. Cross, "Dielectric and Piezoelectric Properties of Tungsten Bronze Lead Barium Niobate ($Pb_{1-x}Ba_xV_2O_6$) Single Crystals," presented at the 5th European Meeting on Ferroelectrics, Sept. 26-30, 1983, Benalmadena, Spain.

4. J.R. Oliver and R.R. Neurgaonkar, "Ferroelectric Solid Solutions Based on the Tungsten Bronze Structure," presented at the 86th Annual Meeting of the Am. Ceram. Soc., April 30-18, 1984, Pittsburgh, PA (invited paper).

5. J.R. Oliver and R.R. Neurgaonkar, "Morphotropic Tungsten Bronze Solid Solutions," presented at the 37th Pacific Coast Regional Meeting of the Am. Ceram. Soc., October 28-31, 1984, San Francisco, CA.

6. R.R. Neurgaonkar, W.K. Cory and J.R. Oliver, "Ferroelectric Tetragonal Tungsten Bronze Crystals for Optoelectronic Applications," presented at the 37th Pacific Coast Regional Meeting of the Am. Ceram. Soc., October 28-31, 1984, San Francisco, CA.

9.0 REFERENCES

1. S.T. Liu and R.B. Maciolek, IEEE Technical Digest of 1973 Int. Electron. Device Meeting, Washington, DC, 259 (1973).

2. S.T. Liu and R.B. Maciolek, J. Electron. Mat. 4, 91 (1975).

3. S.T. Liu, J.D. Zook and D. Long, Ferroelectrics 9, 39 (1975).

4. J.E. Geusic, H.J. Levenstein, J.J. Rubin, S. Singh and L.G. Van Uitert, Appl. Phys. Lett. 11, 269 (1967).

5. L.G. Van Uitert, J.J. Rubin and W.A. Bonner, IEEE J. Quantum Electron. 4, 622 (1968).

6. L.G. Van Uitert, H.J. Levinstein, J.J. Robin, C.D. Capio, E.F. Dearborn and W.A. Bonner, Mat. Res. Bull. 3, 47 (1968).

7. R.L. Barns, J. Appl. Cryst. 1, 290 (1968).

8. K. Nagata, T. Yamazaki and K. Okazaki, Proc. of the 2nd Int'l Meeting on Ferroelectric Mat. and Their Applications, 251 (1979).

9. K. Megumi, H. Kozuka, M. Kobayashi and Y. Furuhata, Appl. Phys. lett. 30, 631 (1977).

10. G.A. Rakuljic, A. Yariv and R.R. Neurgaonkar, to be published (1985).

11. J. Feinberg, D. Heiman, A.R. Tanguay, Jr., and R.W. Hellwarth, J. Appl. Phys. 51, 1297 (1980).

12. N.V. Kukhtarev, V.B. Markov and S.G. Odulov, Opt. Comm. 23, 338 (1977).

13. N.V. Kukhtarev, V.B. Markov, S.G. Odulov, M.S. Soskin and U.L. Vinetskii, Ferroelectrics 22, 949 and 961 (1979).

14. N.V. Kukhtarev, Sov. Tech. Phys. Lett. 2, 438 (1976).

15. E.V. Bursian, G. Girshbert and A.V. Ruzhnikov, Phys. Stat. Sol. (b) 74, 689 (1976).